Title
Mixing and trapping of dissolved CO2 in deep geologic formations with shale layers

Authors
Agartan, Elif
Cihan, Abdullah
Illangasekare, Tissa H
et al.

Publication Date
2017-07-01

DOI
10.1016/j.advwatres.2017.04.014

Peer reviewed

Mixing and trapping of dissolved CO_2 in deep geologic formations with shale layers

Author links open overlay panelElifAgartan[ac]AbdullahCihan[b]Tissa H.Illangasekare[a]QuanlinZhou[b]Jens T.Birkholzer[b]
Show more

https://doi.org/10.1016/j.advwatres.2017.04.014Get rights and content

Abstract

For dissolution trapping, the spatial variability of the geologic properties of naturally complex storage formations can significantly impact flow patterns and storage mechanisms of dissolved CO_2. The significance of diffusive mixing that occurs in low permeability layers embedded between relatively higher permeability materials was highlighted by Agartan et al. (2015) using a highly controlled laboratory experimental study on trapping of dissolved CO_2 in multilayered systems. In this paper, we present a numerical modeling study on the impacts of low permeability layers on flow and storage of dissolved CO_2 in realistic field-scale settings. The simulator of variable-density flow used in this study was first verified using the experimental data in Agartan et al. (2015) to capture the observed processes. The simulator was then applied to a synthetic, field-scale multilayered system, with 19 sensitivity cases having variable permeability and thickness of the shale layers as well as the source strength and geometry of the source zone of dissolved CO_2. Simulation results showed that the presence of continuous shale layers in the storage system disrupts the convective mixing by enhancing lateral spreading of dissolved CO_2in sandstone layers and retarding the vertical mixing of dissolved CO_2. The effectiveness of trapping of dissolved CO_2 depends on the physical properties of the shale layers and configurations of the source zone. The comparison to homogeneous cases with effective vertical permeability shows that it is important to capture these continuous thin shale layers in a storage formation and include them in the models to enhance dissolution trapping.

1. Introduction

Carbon capture and storage is considered as an important strategy to lower atmospheric loading of CO_2 gas, which may eventually reduce the impacts of global warming and climate change (Benson and Cook, 2005). The goal of geologic CO_2 sequestration is to create stable trapping conditions where CO_2becomes immobilized. Dissolution entrapment is one of the primary trapping mechanisms that increases the storage security in deeper parts of the formation due to increasing density

of CO_2 -rich brine after dissolution compared to brine (Benson and Cook, 2005). In relatively permeable homogeneous formations where convection is the dominant transport and mixing mechanism, the trapping strategy should be aimed to maximize the amount of dissolved CO_2 in contact with the host rock and its residence time to enhance potential for mineralization (Agartan et al., 2015). However, heterogeneity of the formation plays a key role on stability of trapping (Bachu, 2008, Bradshaw et al., 2007, De Silva et al., 2012, Farajzadeh et al., 2011, Nield and Simmons, 2007, Ranganathan et al., 2012, van der Meer, 1993). For example, when there are distinct layers in the formations, relatively lower permeability zones might contribute to the long-term storage of dissolved CO_2due to slow diffusion rates within them (Agartan et al., 2015).

The role of vertical permeability variation on mixing and storage in multilayered systems has been investigated for a range of applications in subsurface contamination, heat convection, and mixing of fresh and salt water (e.g. Chapman and Parker, 2005, McKibbin and O'Sullivan, 1980, Schincariol et al., 1994, Vithanage et al., 2012). In the studies of heat flow in multilayered systems where diffusion contributes to heat distribution in low conductive zones, it has been shown that an increasing number of layers made the system behavior similar to that of an anisotropic homogeneous porous mediumin the context of temperature distribution (McKibbin and O'Sullivan, 1980, McKibbin and Tyvand, 1982, McKibbin, 1986). In contrast, an experimental study of mixing of fresh and salt water indicated the significance of permeability variations in a layered medium where a half order of magnitude or less decrease in permeability could lead to mass accumulation along layer interfaces (Schincariol and Schwartz; 1990). The role of low-permeability zones for storing dissolved chemicals has been known for decades in the context of groundwater contamination, as solute diffusing into low permeability layers behaves like a continuous source of contamination due to back diffusion into adjacent permeable zones (e.g. Chapman and Parker, 2005, Chapman et al., 2012, Parker et al., 2004, Wilking et al., 2012). Parker et al., (2008) showed through a numerical modeling study that a single thin clay bed with 0.2 m thickness could store a significant amount of dissolved TCE mass for several years. This underlines the potentially large storage capacity of clay beds. Tsunami-like events also cause gravitational instabilities in subsurface formations due to the release of heavier seawater into unconfined fresh water aquifers which contaminates drinking and/or irrigation water resources. Low permeability zones present in the formations can store salt water through diffusion, which influences the timescales of aquifer contamination and corresponding remediation processes (Illangasekare et al., 2006).

Likewise, during CO_2 storage, the presence of low permeability layers in a storage reservoir can contribute to the long term trapping of dissolved CO_2, as demonstrated for example in several simulation studies. A numerical study on the impact of horizontal discontinuous shale lenses on convection showed that the presence of shale lenses decreases the onset time of convective mixing compared to a homogeneous case with the same effective permeability (Green et al., 2009, Green and Ennis-King, 2010). Increasing horizontal and vertical apertures between the barriers tend to enhance mass flux into the domain, whereas longer barriers tend to decrease it (Elenius and Gasda, 2013). The results of numerical models on convection in dual-layer systems with a low permeable layer on top of a high permeable layer and vice versa showed that the vertical flow was dominated by natural convection for both of the cases, and the reduction in vertical permeability decreased the effects of convective mixing (Farajzadeh et al., 2008).

The effects of low permeability zones on dissolution trapping of CO_2-analog fluids in a layered medium were investigated further using a set of small tank experiments conducted under identical initial and boundary conditions (Agartan et al., 2015, Agartan Karacaer, 2015). The experimental results showed that diffusive flow was the dominant mixing mechanism in low permeability layers and these layers could effectively trap the dissolved CO_2-analog fluid. This process under actual sequestration conditions can eventually enhance stable trapping of injected CO_2. Built on these referred previous studies, the goal of this study is to evaluate the applicability of the previous experimental findings observed in small tank experiments by Agartan et al. (2015) in a field-scalesetting, focusing on the influence of shale layer and source zone properties on flow and storage of dissolved CO_2. An in-house numerical model was developed and employed to simulate miscible flow of a binary fluid mixture with density and viscosity variations to understand and assess the influences of the shale layer geometry and hydraulic properties on flow and transport of dissolved CO_2 for both laboratory-scale and field-scale analyses. The small tank experiments presented in Agartan et al. (2015) were simulated to test the ability of the model to represent convective and diffusive flow regimes observed in the experiments. The influences of shale layer permeability and thickness, and source strength and source zone geometry on flow and trapping of dissolved CO_2 in a multilayered system were investigated at field-scale settings.

2. Numerical modeling and verification

A numerical simulator of single-phase, variable-density and variable-viscosity flow and two-component transport is employed to improve the understanding of diffusive and convective mixing processes in trapping of dissolved CO_2 at both laboratory and field scales. The in-house simulator is based on solutions of the coupled continuity equation, advection-diffusion equation, and Darcy equation (Bear, 1972):

$$\partial(\phi\rho)\partial t+\nabla(\rho q)=0 \quad (1)$$

$$\partial(\phi\rho w)\partial t+\nabla(\rho wq-\phi D\rho\nabla w)=0 \quad (2)$$

$$q=-k\mu(\nabla P+\rho g\nabla z) \quad (3)$$

where ρ is the density of the solution (kg/m^3), w is the CO_2 mass fraction (−), $P$is the pressure (Pa), **q** is the Darcy flux (m/s), ϕ is the porosity (−), D is the diffusion coefficient (m^2/s), **k** is the permeability of the porous medium (m^2), $g$is the gravitational acceleration (m/s^2), and μ is the viscosity of the solution (Pa.s). The two coupled non-linear partial differential Eqs. (1)–(2) are discretized by the Finite Volume Method (FVM) and solved by Newton-Raphson (NR) method. At each NR iteration, the linearized system of equations is solved by a preconditioned restarted Generalized Minimum Residual (GMRES) algorithm.

Viscosity of brine, μ, is assumed to be independent of dissolved CO_2 mass fraction (Phillips et al., 1981). Density of the solution, ρ, is a linear function of CO_2 mass fraction and is represented in the model (Duan et al., 2006) using

$$\rho CO2=MWCO2V\phi 103 \quad (4)$$

$$V\phi=37.51-9.585\times10-2T+8.740\times10-4T2-5.044\times10-7T3 \quad (5)$$

$$1\rho=1-w\rho b+w\rho CO2 \quad (6)$$

where ρ_{CO_2} is the partial density of dissolved CO_2 (kg/m^3), MWCO2 is the molecular weight of CO_2 (44.01 g/mole), V_ϕ is the molar volume of dissolved CO_2 (cm^3/g mole), T is the temperature (°C), and ρ_b is the density of brine (kg/m^3) assumed to be constant.

The numerical simulator was verified using the Elder benchmark problem (see Appendix A). We further verified the simulator using the convective and diffusive flow processes observed in the quasi-2D laboratory experimentscarried out by Agartan et al. (2015). In the experiments, the gravitational instabilities and convective fingering were observed and attributed to different factors, including the non-uniform distribution of injected fluid in the source zone due to injection procedure (see Fig. 1), pore-scale heterogeneities, and small-scale heterogeneities caused by sand packing imperfections. To accurately capture convective fingering, a numerical model may require use of very high spatial and temporal resolutions. However, even then, the onset of convection and finger evolution are very sensitive to numerical errors resulting from numerical solution procedure with finite tolerances, and those errors need to be minimized although they

cannot be completely eliminated. Therefore, we conducted series of sensitivity analyses to better understand the effects of the grid resolution and fluctuation (percentage perturbation around mean of a parameter value) strength of porosity and permeability on the onset of convective fingering, with the objective of minimizing numerical errors when performing laboratory- and field-scale simulations. Details of the sensitivity analysis study are presented in Appendix B.

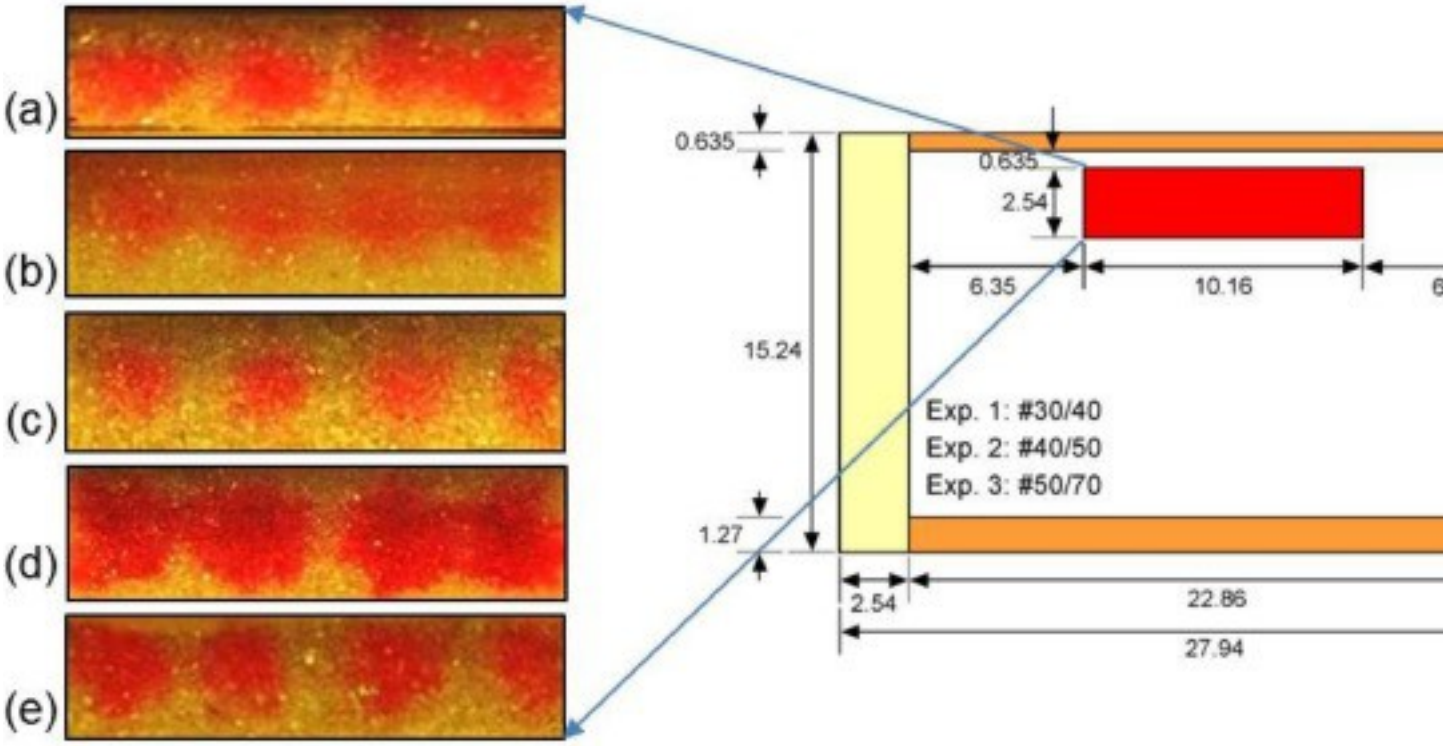

1. Download high-res image (413KB)
2. Download full-size image

Fig. 1. The distribution of the injected fluid in the source zone after injection-extraction period for (a) #30/40, (b) #40/50 and (c) #50/70 homogeneous, and (d) 2nd multilayered system and (e) 3rd (rectangular blocks) heterogeneous small tank experiments (Agartan et al., 2015).

Agartan et al. (2015) studied the convection and diffusion behavior of dissolved CO_2 in homogeneous and heterogeneous porous media using small tank experiments under ambient pressure and temperature conditions. The experiments shown in Fig. 1 were carried out using a surrogate fluid combination that includes water as analog of CO_2 and propylene glycol as analog of brine (PG/W). The density, ρ_{PG}, and viscosity, μ_{PG}, of propylene glycol solutions are functions of water mass fraction, w, as given in Eqs. (7)and (8), respectively (Agartan et al., 2015, Backhaus, 2011), as follows:

(7)ρPG=85.935w3−217.62w2+88.425w+1034.1

(8)μPG=4.496w3exp(−3.8613w)

The synthetic aquifer domain used in the experiments consists of four zones: the main mixing domain, the source zone, the impervious caprock and bedrock(Fig. 1). The main mixing domain is packed either homogeneously using uniform sands or heterogeneously using layers of different sands. Table 1 lists some general properties of the sands used in the experiments. No-flow and no-flux conditions for pressure and concentration are assigned to the left, right, and bottom boundaries. The top boundary is specified using atmospheric pressure and no-transport conditions. The initial concentration of the water within the test domain was zero except within the source zone. Agartan et al. (2015) applied the injection/extraction method to create the source zone using four 1 ml syringes. Total net injected volume of food-dyed water was 1 ml for each experiment. After the injection-extraction period, small-scale heterogeneities at coarse/fine sand interfaces and imperfections of packing resulted in highly non-uniform distribution of the fluid mixture in the source zone. Therefore, the final distribution of the colored fluid mixture was different among the different experiments as shown in Fig. 1. The final distribution of the mixture in the source zone during each experiment was captured as an image and mapped into the numerical grid within the area of the colored fluid mixture to specify initial water mass fraction. Following the sensitivity analyses in Appendix B, we added a relative fluctuation of 10%, greater than the critical value 2.0%, to the sand porosity values in the numerical model to ensure that the fluctuations overcome the effects of the numerical errors while not creating large artificial heterogeneities. The source zone was discretized with the critical grid resolution of 0.0635 cm to accurately capture the initiation of convection. The grid sizes were increased slightly toward the sides of the tank. An effective diffusion coefficient of 8×10^{-11} m^2/s was used.

Table 1. Properties of the sands used in Agartan et al.'s (2015) experiments.

Sand	Permeability, k ($\times 10^{-10}$) (m^2)	Porosity, ϕ (−)
#12/20	3.830[a]–5.230[b]	0.318[a]
#20/30	2.340[a]–2.780[b]	0.320[a]
#30/40	1.080[a]–1.520[c]	0.325[a]
#40/50	0.530[a]–0.736[c]	0.334[a]
#50/70	0.311[a]–0.346[c]	0.372
#50w	0.170[d]–0.258[d]	0.301[d]

a

Smits et al. (2010).

b

Wietsma et al., (2009).

c

Schroth et al., (1996).

d

Sakaki and Illangasekare (2007).

e

Zhang et al., (2008).

Fig. 2 presents the snapshots of the simulated concentration contours for the injected fluid compared to the visual images of the dyed water captured during the experiments with homogeneous and multilayered settings. In the homogeneous experiment, the main mixing domain was packed with #30/40 sand of medium permeability (Table 1). Figs. 2a and b show that the model represents reasonably well the time-dependent convective fingering and spreading of the plume observed during the homogenous tank experiments. On the other hand, the alternating layers of coarse, medium and fine sands in the order of #30/40, #50w, #20/30, #40/50, and #30/40 were utilized in the multilayered experiment. Figs. 2c and e show that the plume accumulates and subsequently spreads laterally above the lower permeability layers as it continues to sink down slowly. Both the modeling and experimental results show that the finger fronts widen after they pass through the relatively lower permeability layers. All these comparisons indicate that qualitatively the model is able to well represent all these observed processes.

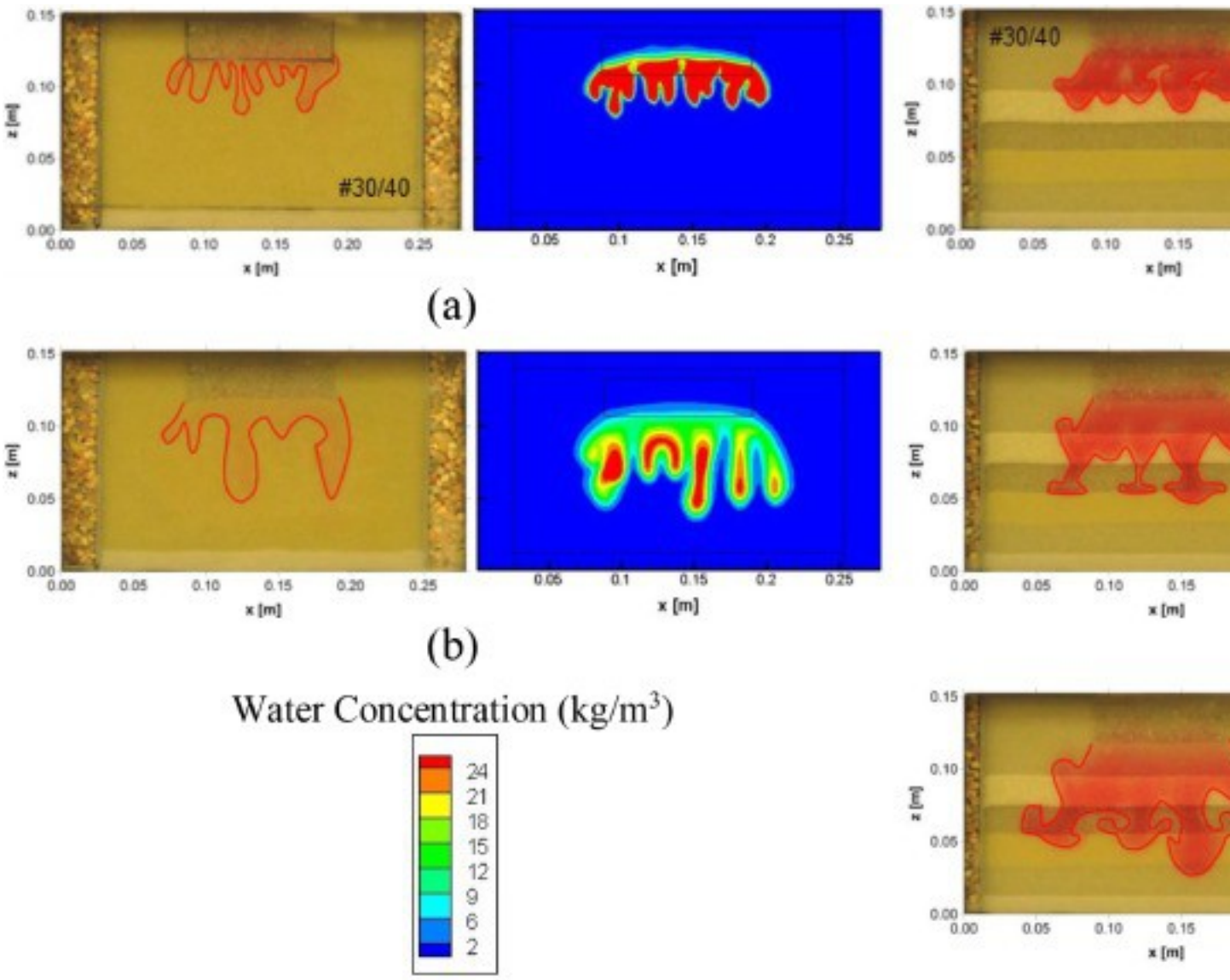

1. Download high-res image (654KB)
2. Download full-size image

Fig. 2. The comparison of experimental (Agartan et al., 2015) and simulation results for the 1st homogeneous (#30/40 sand) experiment: (a) at 1.5 days, (b) at 7 days, and for the 2nd heterogeneous (multilayered heterogeneity) experiment: (c) at 3 days, (d) at 9 days, (e) at 18 days.

Fig. 3a and c compare the predicted propagation of the longest finger from the bottom of the source zone with the observed results for both homogeneous and multilayered experiments. The predicted finger lengths generally agree well with the observed values in the homogeneous tanks experiments with #30/40 and #50/70 sands, and the multilayered case. The deviations between the model predictions and the observations

appear larger for the #40/50 sand homogeneous tank experiment. The model predictions of the plume center of mass (first spatial moment) in vertical z-direction are also in agreement with the experimental results where Agartan et al. (2015) determined concentration distribution of water at each experiment using image processing method. Similarly, the first moment comparisons show some deviations for the sand #50/70 experiment (Fig. 3b). The slight mismatches between the experimental and numerical modeling results for the homogeneous experiments (Fig. 3a and b) could be attributed to pore-scale heterogeneity in the main mixing domain due to packing imperfections such as tightness/looseness of the packing and mixing of the different sized sands. Imperfections in packing and mixing of the main domain and source zone sands might trigger early or late onset of convection in the system compared to the numerical modeling results. The results in Figs. 3c and d highlight the dependence of vertical spreading on the permeability of the horizontal layers for the multilayered system. In this system, the fingers propagate much faster vertically in the higher permeability layers with #30/40 and #20/30 sands, compared to the lower permeability layers with #50w and #40/50 sands. The simulation results of the experiments show that the numerical model is able to capture the important flow and transport processes.

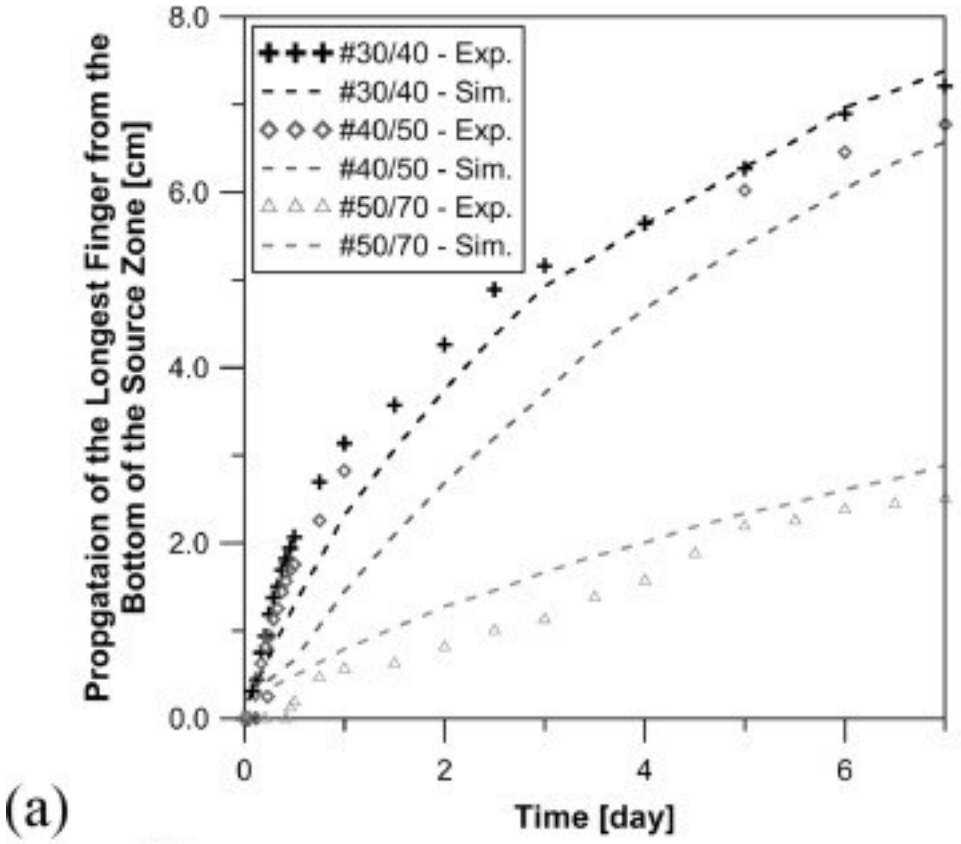
Propgataion of the Longest Finger from the Bottom of the Source Zone [cm]
Time [day]
#30/40 - Exp.
#30/40 - Sim.
#40/50 - Exp.
#40/50 - Sim.
#50/70 - Exp.
#50/70 - Sim.
0.0
2.0
4.0
6.0
8.0
0
2
4
6

(a)

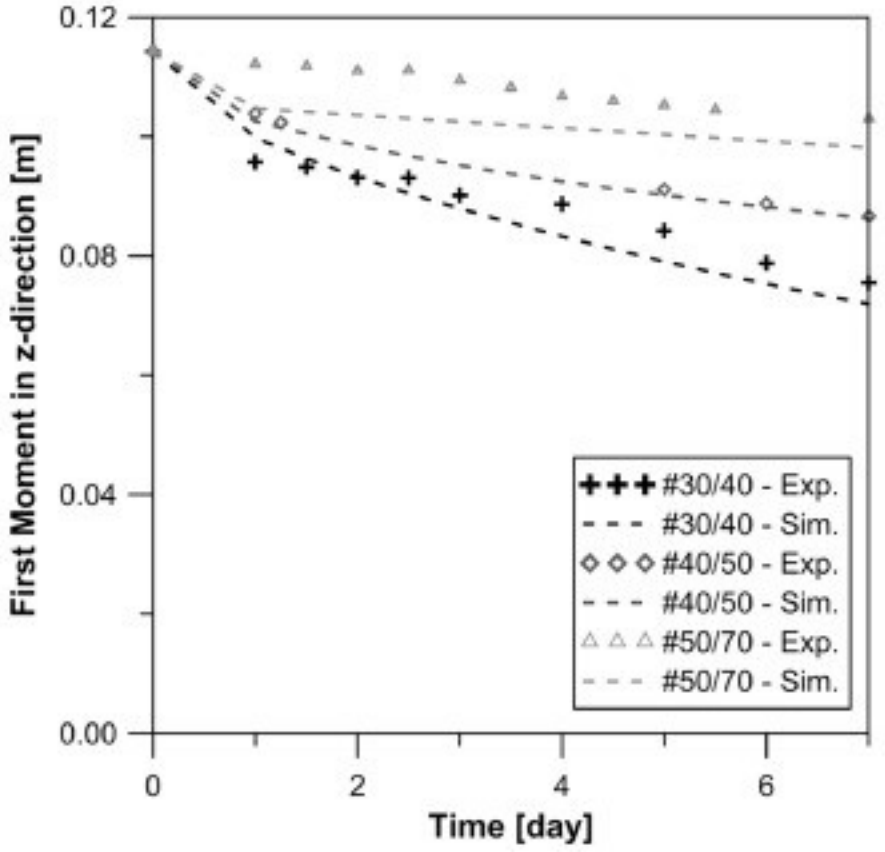
First Moment in z-direction [m]
Time [day]
#30/40 - Exp.
#30/40 - Sim.
#40/50 - Exp.
#40/50 - Sim.
#50/70 - Exp.
#50/70 - Sim.
0.00
0.04
0.08
0.12
0
2
4
6

(b)

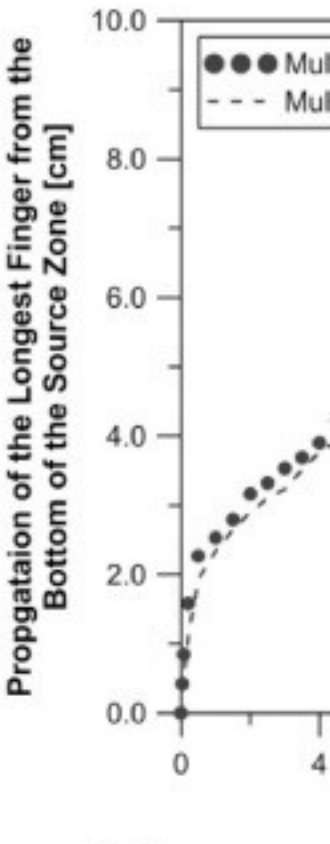
Propgataion of the Longest Finger from the Bottom of the Source Zone [cm]
0.0
2.0
4.0
6.0
8.0
10.0
0
4

(c)

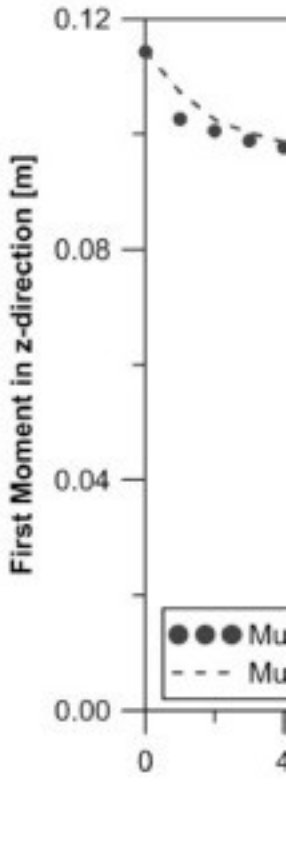
First Moment in z-direction [m]
0.00
0.04
0.08
0.12
0
4

(d)

1. Download high-res image (532KB)
2. Download full-size image

Fig. 3. Comparison of the experimental (Agartan et al., 2015) and modeling results for homogeneous and multilayered heterogeneous experiments: Propagation of the tip of the longest finger for (a) homogeneous and (c) heterogeneous cases, and the first moments in z-direction for (b) homogeneous and (d) heterogeneous cases.

3. Model development for field-scale simulations

The model verification presented above takes advantage of the improved understanding of the observed processes at fine scales and high resolutions from the laboratory experiments performed under the controlled initial and boundary conditions, using the mixture of the surrogate fluids (PG/W) with density differences similar to the brine with dissolved CO_2 under reservoir pressure and temperature conditions. The experiments have some limitations: (1) the PG/W fluid combination is less stable than the CO_2/brine system and may influence fingering patterns (e.g. growth rate of fingers) (Emami-Meybodi et al., 2015, Raad and Hassanzadeh, 2015, Raad et al., 2016), and (2) the permeability contrasts of the coarse and fine sands used in the laboratory experiments are much smaller than those of the sandstone and shale in real CO_2 storage reservoirs. The confidence in the numerical modeling built through the verification allows us to investigate the transport of dissolved CO_2in realistic field conditions. The main goal of the field-scale modeling is to further improve the understanding of the impact of natural lower permeability layers on flow and storage of dissolved CO_2 in multilayered reservoir systems.

Two types of multilayered systems can be used for CO_2 storage. The first is a thick sandstone reservoir with a number of intra-formation shale layers that are thin and continuous. One example of this type system is the Utsira formation in the North Sea at the Sleipner site (Chadwick et al., 2004, Zweigel et al., 2004, Arts et al., 2008). The other type is a sequence of sandstone and shale layers whose thickness vary in the vertical direction, and the multiple sandstone layers are used for simultaneous injection to enhance injectivity and storage capacity. One example of the second type is the Shenhua Ordos Project (Li et al., 2016, Zhang et al., 2016). Note that these shale layers are not thicker aquitards of a multilayered aquifer-aquitard system (Cihan et al., 2011), such as the Texas Gulf Coast basin (Nicot, 2008), the Dakota aquifer system in South Dakota (Konikow and Neuzil, 2007), and the coastal plain aquifer systems in Virginia (Konikow and Neuzil, 2007). For the multilayered storage systems, the shale layers can

significantly influence the migration of the dissolved CO_2, depending on their permeability, thickness and lateral extent in the systems.

We created a 2D numerical model for investigating transport of dissolved CO_2through a multilayered reservoir system. The model domain is 150 m in height and 240 m in length. No-flow and no-flux boundary conditions for pressure and concentration were assigned to left, right, and bottom boundaries. The top boundary was specified as constant reservoir pressure of 9 MPa (Johnson et al., 2004, Nooner et al., 2007) and no-flux condition for transport. The initial concentration of CO_2 within the model domain was zero except within the source zone (Fig. 4). Average temperature was assumed to be 36.2°C (Johnson et al., 2004, Nooner et al., 2007).

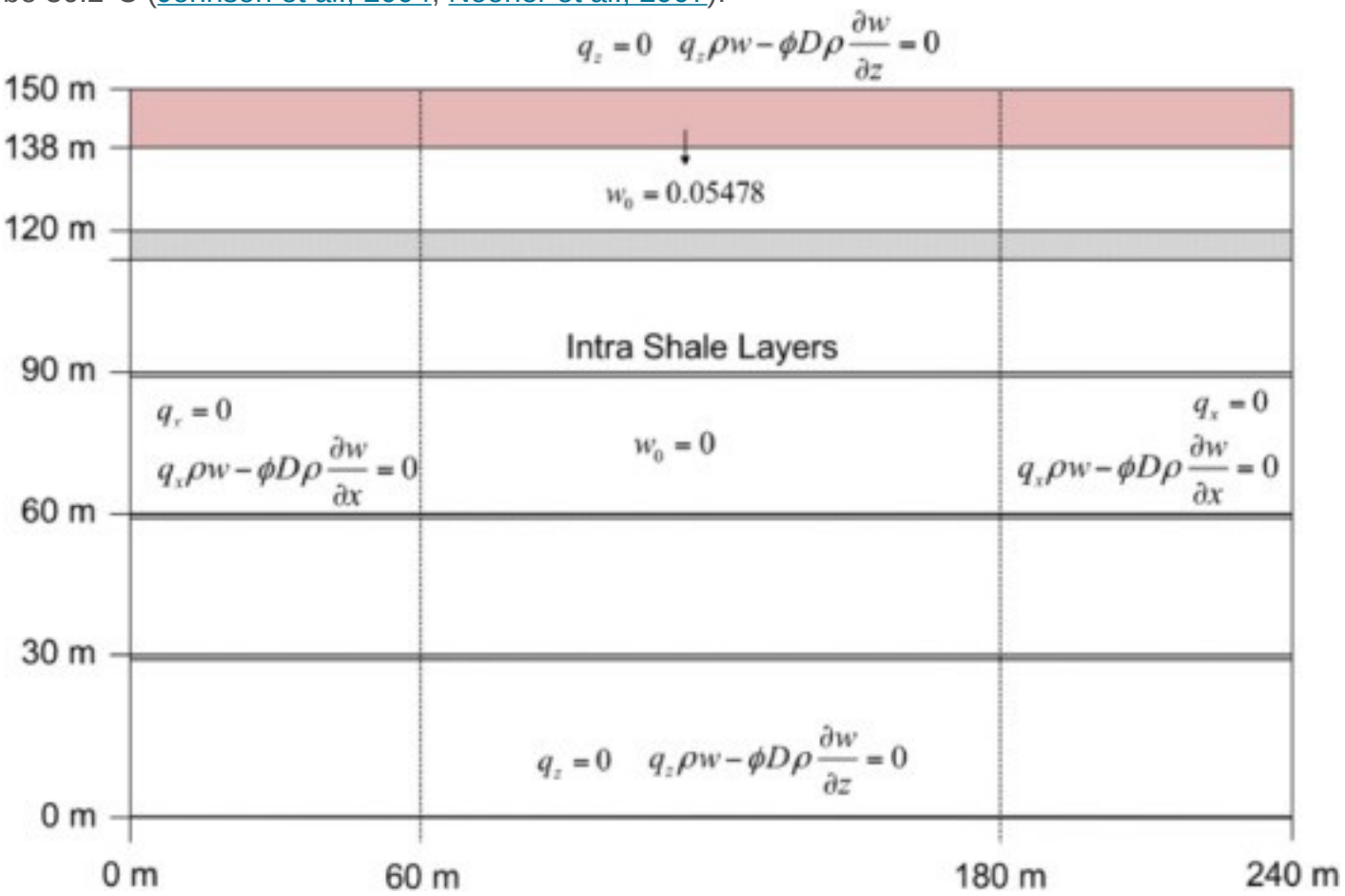

1. Download high-res image (218KB)
2. Download full-size image

Fig. 4. The model domain to study the role of lower permeability shale on flow and storage of dissolved CO_2.

The model domain consists of five horizontal composite layers, as shown in Fig. 4. Each composite layer is 30 m thick and includes a sandstone layer and an overlying shale

layer. Only the uppermost sandstone does not have an overlying shale layer. The sandstone and shale layers are assumed to be horizontally continuous. The thicknesses of three sandstone and shale layers from the bottom of the domain are kept constant at 29 m and 1 m, respectively. The thickness of the uppermost sandstone layer is 30 m. The thicknesses of the second sandstone layer and the uppermost shale layer vary. We used similar permeability, porosity, diffusion coefficient, and average temperature and pressure values from the Utsira formation at the Sleipner site. The permeability and porosity of the sandstone layers are specified as 2×10^{-12} $m^2$and 35%, respectively (Herrera et al., 2010, Torp and Gale, 2004). While the porosity of the shale layers is kept constant at 5%, their permeability is varied with different cases (Johnson et al., 2004). The molecular diffusion coefficient is set to 2.06×10^{-9} m^2/s (Lindeberg and Bergmo, 2003). For all the following simulations, a 12-m thick source zone containing dissolved CO_2 at solubility limit of CO_2 in brine ($w_0 = 0.05478$) under reservoir pressure and temperature conditions is assumed either to be placed instantaneously or to exist continuously under the caprock (i.e., the top boundary) (Lindeberg et al., 1999). Density, viscosity, and compressibility of the brine were calculated using 3.05% salinity of the brine (by weight) (Grimstad et al., 2009) as 1018.53 kg/m^3, 0.73×10^{-3} Pa.s and 4.1×10^{-10} 1/Pa, respectively. Solubility of supercritical CO_2 in brine was determined to be 1.2575 mol/kg using the equation of state developed by Duan and Sun (2003) and Duan et al., (2006). The 2D numerical model domain is represented by a structural mesh containing 80 horizontal and 89 vertical grid blocks. The grid sizes become smaller around sand- shale interfaces. Mineralization is neglected in all of the simulations. Employing the numerical simulator that was verified against experimental data, we investigated the sensitivity of convective mixing and storage of dissolved CO_2 with respect to shale layer properties as well as source zone configurations. For each case, one parameter was changed in order to explore its influence on the results. Each case was labeled by the capital letter “C (i, j)” (Table 2). The first index ‘i’ denotes the cases with different shale layer permeability, and the second index number ‘j’ denotes the other specific conditions for different source properties and shale layer thicknesses that were simulated. Table 2 lists three shale layer permeability (k_{shale}) cases (i = 1–3) and seven other specific conditions (j = 1–7). These seven specific conditions investigated are: (1) instantaneous release with 1 m thick uppermost shale layer and full-length source, (2) instantaneous release with 6 m thick uppermost shale layer and full-length source, (3) instantaneous release with average vertical permeability and full-length source, (4) instantaneous release with 10 m thick uppermost shale layer and full-length source, (5) instantaneous release with 6 m thick uppermost shale layer and half-length

source, (6) continuous release with 6 m thick uppermost shale layer and full-length source, and (7) continuous release with 6 m thick uppermost shale layer and half-length source. For example, C(1, 5) represents the case with 3×10^{-14} m^2shale layer permeability, 6 m thick uppermost shale layer, instantaneous release of the source from the half-length source zone. Fig. 4 shows the typical initial and boundary conditions used in the analyses. Note that the uppermost shale layer is between the uppermost composite layer with a source zone and the second composite layer from the top boundary, and the thickness of this shale layer controls the mass flux of dissolved CO_2 into the underlying portion of the reservoir system.

Table 2. Shale layer and source zone properties with their corresponding case numbers (C).

Permeability of shale layers, k_{shale} (m^2)	**Thickness of uppermost shale layer, $H_{uppshale}$ (m) (instantaneous release of full-length source)**			**Source strength ($H_{uppshale}$ = 6 m)**				
	1 (1)	**6**		**10** (4)	**Instantaneous release**		**Continuous release**	
		With shale layers, $H_{uppshale}$ = 6 m (2)	**Average vertical permeability for $H_{uppshale}$ = 6 m (k_{avg})** (3)		**Full-length** (2)	**Half-length** (5)	**Full-length** (6)	**Half-length** (7)
3×10^{-14} (1)	C(1, 1)	C(1, 2)	C(1, 3)	C(1, 4)	C(1, 2)	C(1, 5)	C(1, 6)	C(1, 7)
3×10^{-15} (2)	C(2, 1)	C(2, 2)	C(2, 3)	C(2, 4)	C(2, 2)	–	C(2, 6)	–
3×10^{-16} (3)	C(3, 1)	C(3, 2)	C(3, 3)	C(3, 4)	C(3, 2)	C(3, 5)	C(3, 6)	C(3, 7)

4. Results

Based on the analyses of the cases in Table 2, we observed several common transport features after the release of dissolved CO_2 from the source zone either instantaneously or as a continuous source (Fig. 4). These common features are explained below, as an example, for case C(3, 2) with 3×10^{-16} m^2shale layer permeability, 6 m thick uppermost shale layer, full-length source, and instantaneous release of dissolved CO_2. At early times, heavier brine with dissolved CO_2 in the source zone creates gravitational instabilities leading to generation of convective fingers (see Fig. 5a). The onset of convection for this particular case is about 1 year. Fig. 5b indicates that dissolved CO_2 reaches to the uppermost shale layer in less than 5 years. The uppermost shale layer slows down vertical flow and leads to lateral spreading of the denser brine

along sandstone and shale boundary (Fig. 5c). As the lateral spreading continues, mainly diffusion process proceeds to carry dissolved mass into the shale layer. The diffusive mixing in the shale layers contributes to the storage of CO_2 in the uppermost sandstone layer. When the dissolved CO_2 in the uppermost shale layer reaches to the second sandstone layer by gravitational flow and mostly diffusion, some convective fingers appear to form in the underlying sandstone layer at about 1600 years (Fig. 5d). The similar reformation of the fingers as they pass through the deeper sandstone layers from the overlying shale layers are observed at even longer times albeit weaker than the convective fingers in the upper zones. As a result, less and less mass migrates into deeper zones leaving behind significant mass in the upper layers. The observed large-scale features are similar to those observed in the laboratory experiments, but the time scales of the field-scale features are in the order of years to over 1000 years. For all of the cases, the timing and intensity of each process strongly depend on the properties of shale layers and source zone. The effects of these properties are further explained in the following sections.

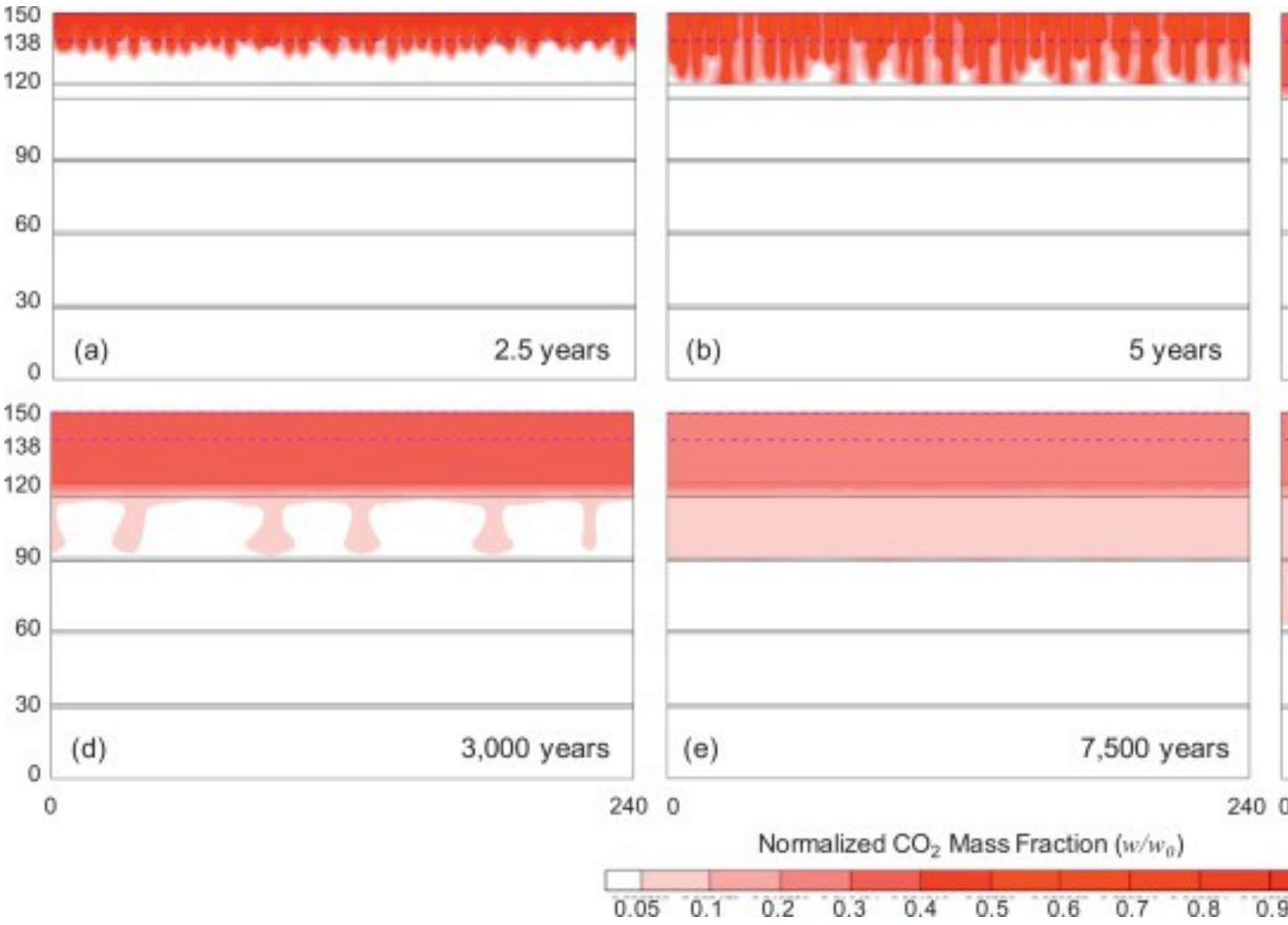

1. Download high-res image (376KB)
2. Download full-size image

Fig. 5. The simulation results of the case C(3, 2): (a) convective fingering in the uppermost sandstone layer at t_1 = 2.5 years, (b) merging of the fingers and lateral spreading at sandstone and shale boundary at t_2 = 5 year, (c) diffusion of dissolved CO_2into and within the uppermost shale layer at t_3 = 1000 years, (d) convective fingering in the second sandstone layer at t_4 = 3000 years, (e) diffusion of dissolved CO_2 into and within the second shale layer at t_5 = 7500 years, and (f) convective fingering in the third sandstone layer at t_6 = 12,000 years.

4.1. Properties of the shale layers

We studied three different shale layer permeabilities (3×10^{-14} m^2, $3 \times 10^{-15}$$m^2$ and 3×10^{-16} m^2) and three different uppermost shale layer thicknesses (1 m, 6 m and 10 m) (Figs. 6 and 7). Fig. 6a shows the simulation results of the cases with 6 m thick uppermost shale layer having different permeabilities (C(1, 2), C(2, 2), and C(3, 2)

in Table 2). The effects of the uppermost shale layer thickness on flow and storage are summarized in Fig. 6b for the cases with 3×10^{-16} m^2 shale layer permeability (C(3, 1), C(3, 2), and C(3, 4)).

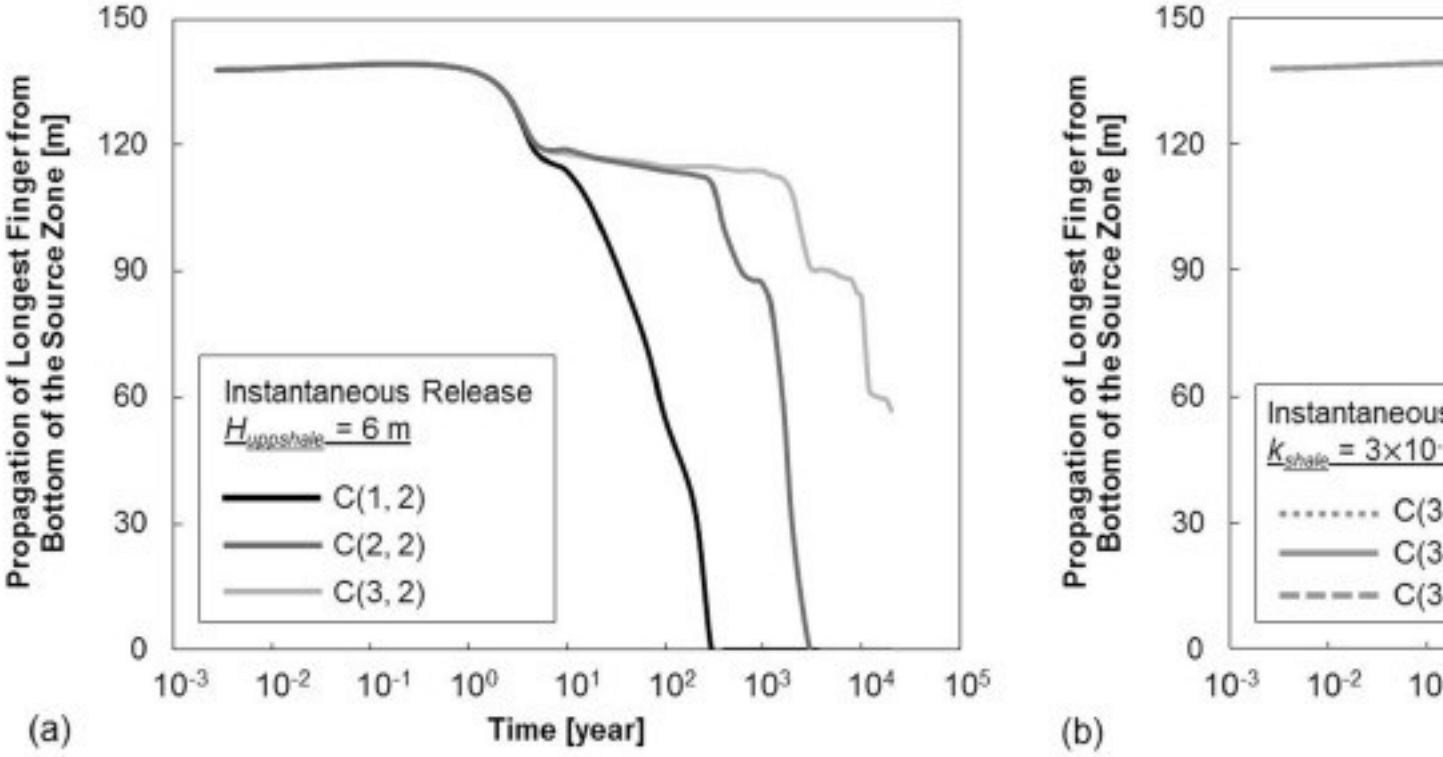

1. Download high-res image (291KB)
2. Download full-size image

Fig. 6. Propagation of longest finger from bottom of the source zone with time for analyses of (a) shale layer permeability and (b) uppermost shale layer thickness.

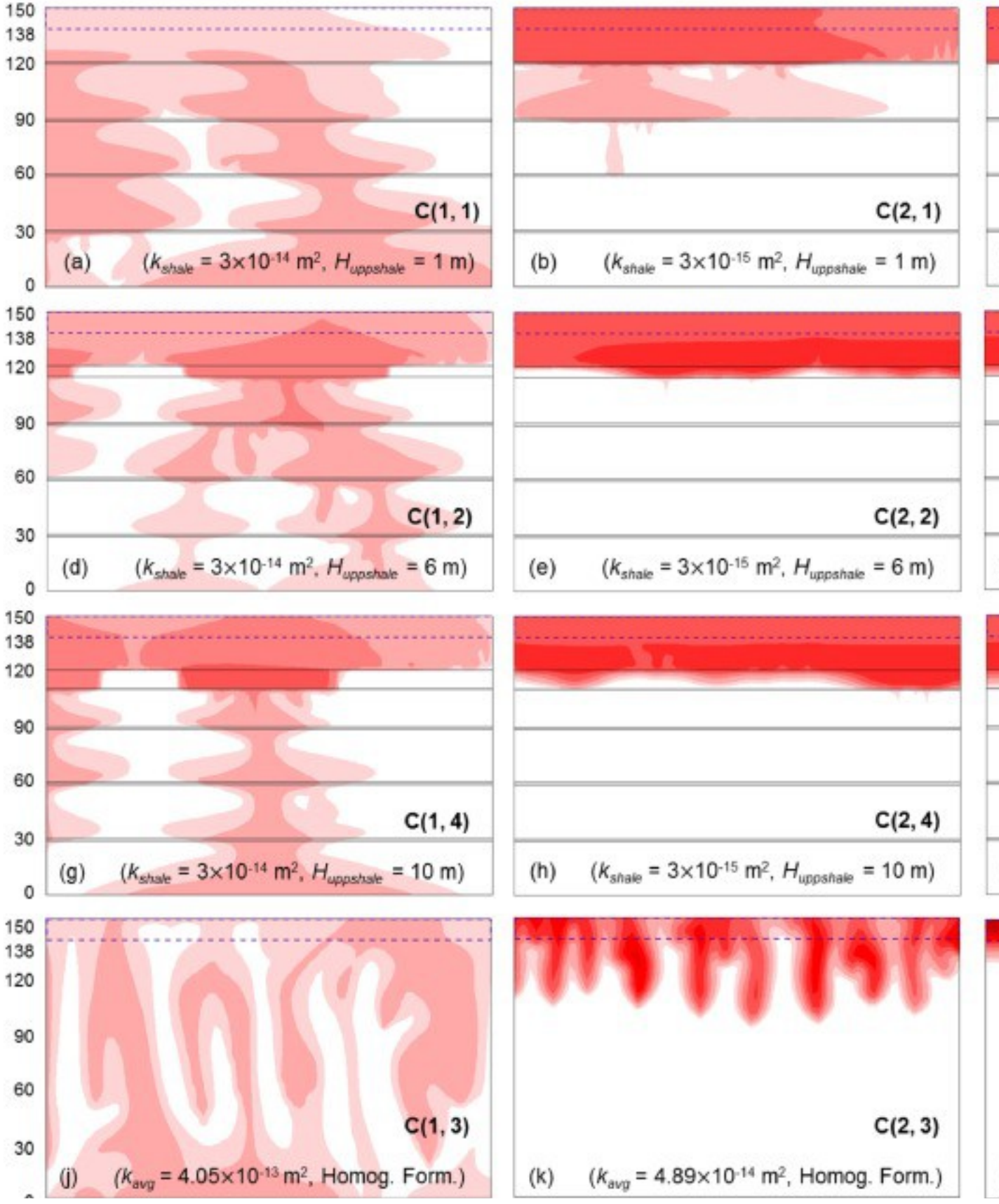
150
138
120
90
60
30
0
C(1, 1)
(a) (k_{shale} = 3×10^{-14} m^2, $H_{uppshale}$ = 1 m)
C(2, 1)
(b) (k_{shale} = 3×10^{-15} m^2, $H_{uppshale}$ = 1 m)
C(1, 2)
(d) (k_{shale} = 3×10^{-14} m^2, $H_{uppshale}$ = 6 m)
C(2, 2)
(e) (k_{shale} = 3×10^{-15} m^2, $H_{uppshale}$ = 6 m)
C(1, 4)
(g) (k_{shale} = 3×10^{-14} m^2, $H_{uppshale}$ = 10 m)
C(2, 4)
(h) (k_{shale} = 3×10^{-15} m^2, $H_{uppshale}$ = 10 m)
C(1, 3)
(j) (k_{avg} = 4.05×10^{-13} m^2, Homog. Form.)
C(2, 3)
(k) (k_{avg} = 4.89×10^{-14} m^2, Homog. Form.)

1. Download high-res image (1MB)
2. Download full-size image

Fig. 7. The effects of the shale layer permeability (a-i), the thickness of uppermost shale layer (a-i), average vertical permeability (j-l), and source zone strength as instantaneous (a-l) and continuous (m-o) release of the source on the distribution of dissolved CO_2 at 400 years.

The onset of convection occurs at a similar time for all of the cases. This is indicated by an initial decline on the propagation of longest finger graph at about 1 year in Fig. 6a. This initial decline in Figs. 6a and 6b continues up to about 10 years representing convective mixing in the uppermost sandstone layer in this time interval. When the plume reaches to the shale layer at 10 years, the vertical flow of dissolved CO_2 slows down depending on the permeability and thickness of the shale layer. For example, at 400 years, the convective fingering which is observed for the 1 m thick uppermost shale layer in the cases C(2, 1) and C(3, 1) in Figs. 7b and 7c does not appear in the deeper sandstone layers when the shale layer is thicker (C(2, 2), C(2, 4), C(3, 2), and C(3, 4)) in Figs. 7e, f, h and i.

4.2. Source strength and source zone geometry

In this section, we investigated the sensitivity of the source strength (instantaneous or continuous release) and the source zone length for the condition of the 6 m thick uppermost shale layer with varying permeability values (Fig. 8, Fig. 9, Fig. 10). We observed that compared to the instantaneous source releases, the onset of convection occurs at later times in the continuous release cases. As independent from the source strength in the cases C(1, 2) and C(1, 6), the convective fingers reach to the second sandstone layer in 10 years. The continuous supply of dissolved CO_2 speeds up the vertical flow, which leads to earlier convective shutdown at the bottom boundary in 200 years for the case C(1, 6) as opposed to 300 years for the C(1, 2) with the instantaneous source release (Fig. 8a). Convection shutdown is observed at 1200 years for C(2, 6) and 3000 years for C(2, 2). The stepwise vertical spreading is observed in the 3×10^{-16} m^2 shale layer permeability cases (C(3, 2) and C(3, 6)) due to slow diffusion rates into and within the shale layers. The results showed that when the convective shutdown occurs at 14,000 years in C(3, 6), the dissolved CO_2 plume only spread in the 62% of the domain in C(3, 2) (Fig. 8a).

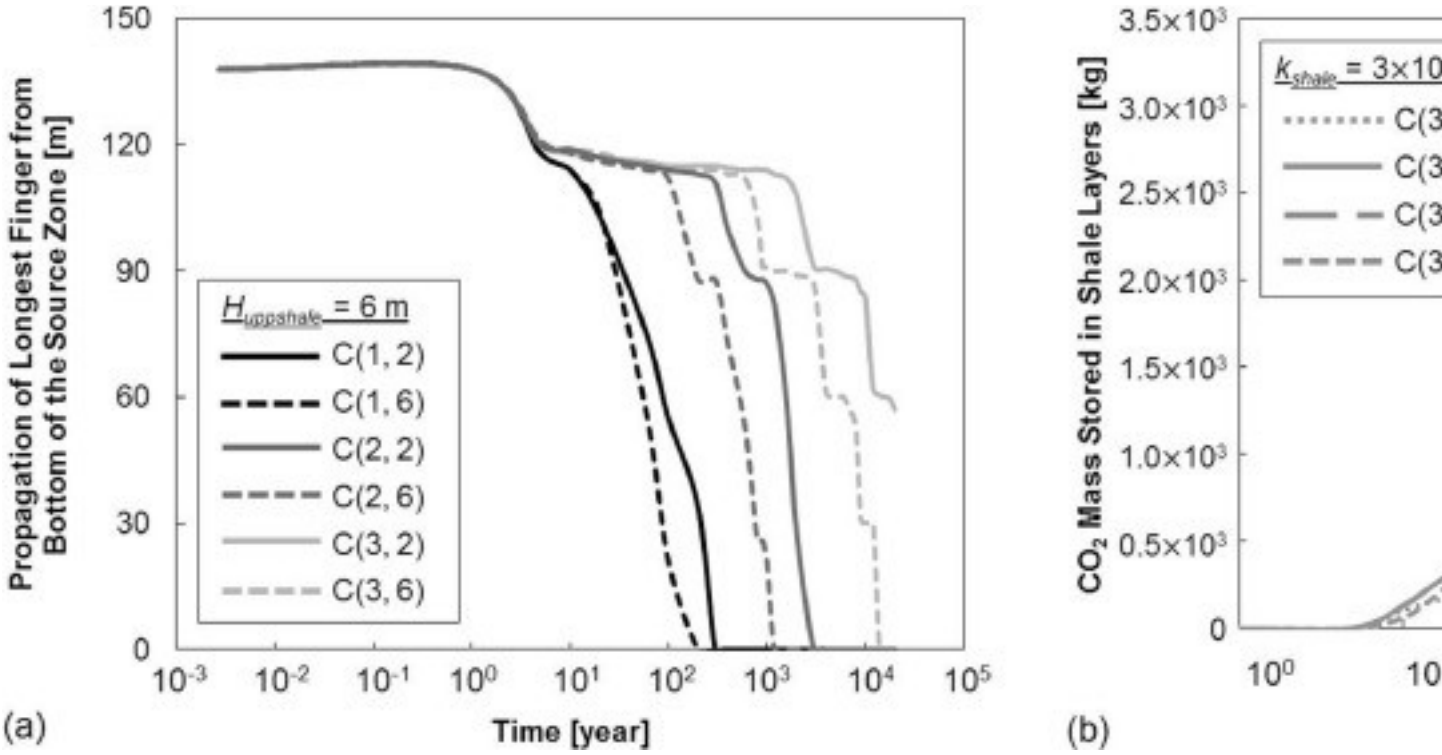

1. Download high-res image (318KB)
2. Download full-size image

Fig. 8. Comparison of instantaneous and continuous source releases: (a) propagation of longest finger from the bottom of the source zone with time for different permeabilities and (b) CO_2 mass stored in shale layers for different uppermost shale layer thicknesses.

The geometry of the source zone is another important factor influencing flow patterns and storage schemes. The results of full- and half-length source zones with instantaneous and continuous source releases are summarized in Figs. 9 and 10. The earlier onset of convection is observed in half-length sources as independent from the source strength. It is followed by faster vertical spreading in the cases C(1, 5) and C(1, 7) with the 3×10^{-14} m^2 shale layer permeability. The stepwise vertical flow is seen in the C(3, 5) and C(3, 7) due to lower permeability of the shale layers.

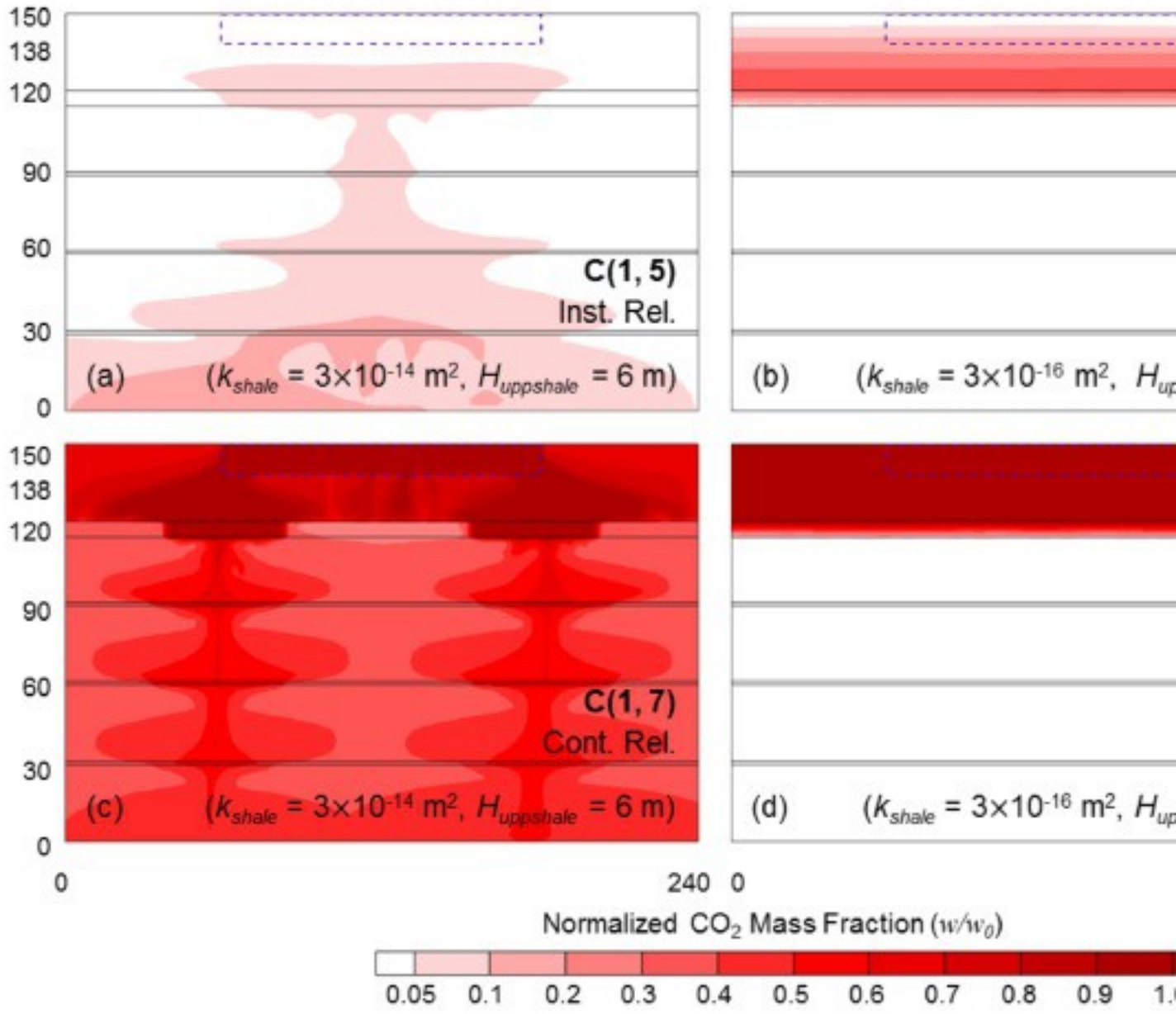

1. Download high-res image (409KB)
2. Download full-size image

Fig. 9. The effects of source geometry (half-length (a-d) and full-length (Fig. 7d, f, m, and o)) and source strength (continuous (c, d, and Fig. 7m and o) and instantaneous (a, b, and Fig. 7d and f) source releases) on the distribution of dissolved CO_2 for different shalepermeability at 400 years.

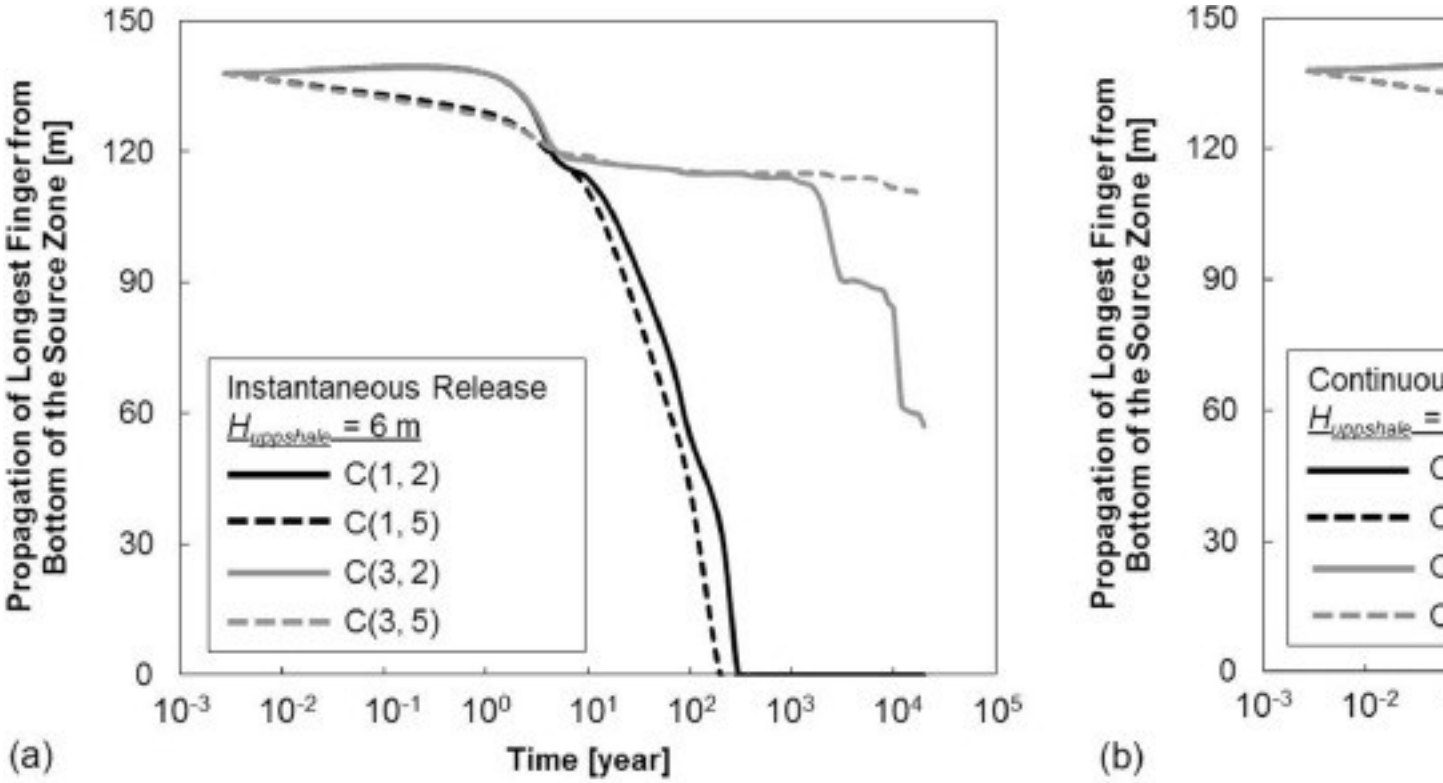

1. Download high-res image (335KB)
2. Download full-size image

Fig. 10. Comparison of full- and half-length sources for (a) instantaneous and (b) continuous source releases.

4.3. Average vertical permeability

The average vertical permeability and porosity of the formations were calculated using harmonic and arithmetic means, respectively, for the different shale layer permeabilities with 6 m thick uppermost shale layers (Figs. 7d–f and 7j–l, Table 2). The same amount of mass was released from the source zone instantaneously. For the homogeneous cases with average vertical permeability, the onset time for convection increases with decreasing effective vertical permeability values (5 years for C(1, 3) and 60 years for C(2, 3)), compared to the multilayered formations (1 year for C(1, 2) and C(2, 2)), as shown in Fig. 11. However, following the onset of convection, vertical flow is faster due to the absence of shale barriers that slow down or block the flow. A more smooth profile of vertical flow is observed in comparison with the stepwise spreading observed in the heterogeneous cases.

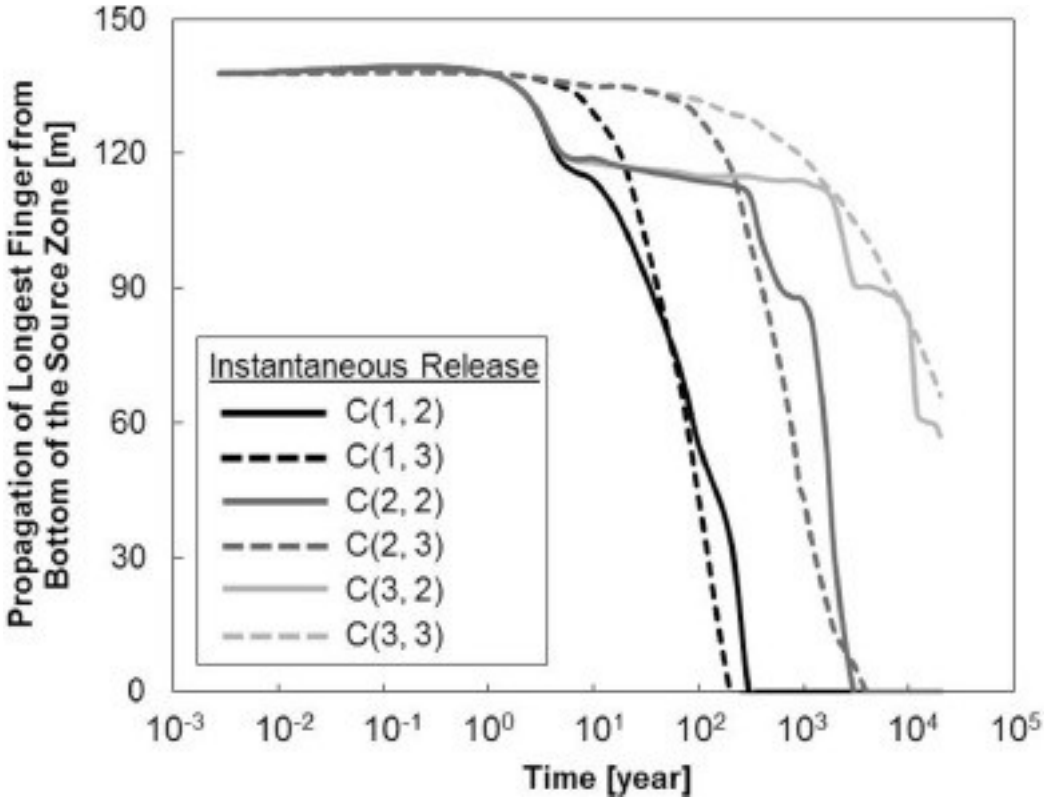

1. Download high-res image (192KB)
2. Download full-size image

Fig. 11. Comparison of propagation of the longest finger from bottom of the source zone with time for multilayered systems and their corresponding homogeneous formations with average vertical permeabilities.

5. Discussion

The presence of any low permeability shale layer retards the vertical flow of dissolved CO_2. The stepwise changes in Fig. 6 indicate the periods with strong convective mixing in the sandstone layers and the periods with significantly decreased convective mixing in the shale layers. During the latter periods, the fingers are getting merged at the layer interfaces, the dissolved CO_2 is slowly diffusing into the shale layers, and the dissolved CO_2 concentrations in the upper sandstone layers are getting homogenized. The similar process occurs in a homogeneous medium when the descending plume reaches to the bottom no-flow boundary, leading to the subsequent decrease in convective flux; the domain begins to fill up with dissolved dense fluid. This is called convective shutdown (Hassanzadeh et al., 2007, Hewitt et al., 2013, Hewitt et al., 2014). In the multilayered systems, we observed that the duration of convective shutdown, i.e., the onset of convective fingering in the deeper sandstone layers, depends on the properties of the

shale layers. The increase in shale layer thickness and the decrease in shale permeability slows down the vertical migration and spreading, while decreasing thickness and increasing permeability significantly contribute to finger generation in the deeper sandstone layers (Figs. 7a–i). For example, the onset times for convection in the second sandstone layers are 80, 1600, and 3750 years for the uppermost shale layer thickness of 1 m, 6 m and 10 m in C(3, 1), C(3, 2), and C(3, 4), respectively. For the same cases, the onset times are 2750, 8750, and 13,000 years, respectively, in the third sandstone layers. For the case C(3, 1), the onset time occurs at 10,000 and 19,200 years at the fourth and the fifth sandstone layers, respectively. As the plume migrates downward, concentration of the dissolved CO_2 at the plume front decreases, leaving a significant portion of the dissolved mass in the layers above. As a result, concentration gradients and diffusive flux within the deeper shale layers decrease, and the onset time for convection increases in the deeper sandstone layers.

The first factor that affects the storage scheme of dissolved CO_2 is shale layer permeability. In Fig. 6, dissolved CO_2 reaches to the system bottom at around 300 and 3500 years in the cases C(1, 2) and C(2, 2), respectively; in other words, the whole domain is started to be used for storage. On the other hand, in C(3, 2), the same mass of dissolved CO_2 is trapped in the 62% of the domain at the end of 20,000 years. The slow transport in the shale layers (convective shutdown) results in accumulation of dissolved CO_2 along the interfaces between the upper sandstone and shale layers, which contributes to the storage of dissolved CO_2 into a smaller volume of the system, i.e., only the top three composite sandstone/shale layers for C(3, 2), as opposed to the whole domain in homogeneous systems. Therefore, the 3×10^{-14} m^2 and 3×10^{-15} m^2 shale layer permeabilities appear to slow down the vertical spreading but they are not small enough to trap dissolved CO_2 for a long period of time. For these cases, the trapping strategy should be to increase the contact area between dissolved CO_2 and the host rock, and the residence time to enhance potential for mineralization. On the other hand, in the case of 3×10^{-16} m^2shale layer permeability, accumulated dissolved CO_2 concentrations become more or less uniform after the convective shutdown, and dissolved CO_2continue to diffuse from this sandstone layer, behaving like a continuous source of CO_2, into the shale layer by effectively trapping CO_2 molecules for an unforeseeable future (Fig. 5 and 7f). Moreover, by the end of 20,000 years, while most of the CO_2 mass leaves the source zone for the cases with 3×10^{-14} m^2 (C(1, 2)) and 3×10^{-15} m^2 (C(2, 2)) shale layer permeabilities, 51.7% of the total CO_2 mass still remains in the uppermost sandstone layer for the case with low permeability (C(3, 2)). This allows storing the same amount of CO_2 in a smaller volume as discussed before.

The second important factor for storage is the thickness of the low permeability shale layers, as shown in Fig. 6. At the end of 20,000 years, for C(3, 1) with 1 m thick uppermost shale layer, dissolved CO_2 plume reaches to the bottom of the formation, spread throughout the whole formation. However, 62% and 59% of the domain is used for storage in the cases with 6 m and 10 m thick uppermost shale layer in C(3, 2) and C(3, 4), respectively. The storage volume decreases with increasing shale layer thickness. In addition, dissolved CO_2mass trapped in the shale layers with 10 m thick uppermost shale layer (C(3,4)) is 6.2 and 1.8 times greater than 1 m (C(3,1)) and 6 m (C(3,2)) thick cases, respectively (Fig. 7c). There is a relationship between shale layer properties and its storage capacity. The thicker and lower permeability shale layers provide stable and long-term trapping in a smaller storage volume.

The third factor is source strength. The sensitivity analyses showed that the onset of convection occurs at later times in the continuous release cases than the cases with instantaneous source releases, because a continuous source with constant dissolved CO_2 concentration prevents generation of convective currents inside the source zone and thus slows down fingering phenomenon in the uppermost sandstone layer. The increased amount of available mass for migration into the system by the continuous source enhances the density gradients and thus more pronounced effects of convection occur after the onset time. The continuous supply of dissolved CO_2 (C(1, 6) and C(2, 6)) speeds up the vertical flow, leading to an earlier convective shutdown at the formation bottom (200 and 1200 years, respectively) as opposed to instantaneous source release cases with 3×10^{-14} m^2 and 3×10^{-15} m^2 shale layer permeabilities (300 and 3000 years for the cases C(1, 2) and C(2, 2), respectively). For the diffusion dominant cases with the 3×10^{-16} m^2 shale layer permeability, the stepwise vertical spreading is apparent in both continuous and instantaneous source releases. The continuous source supply in C(3, 6) decreases the effects of dilution and increases CO_2 concentration gradients. As a result, the onset time for convection shortens in the second sandstone layer beneath the uppermost shale layer. The onset time for convection in the second sandstone layer is 600 years for C(3, 6), compared to 1600 years for C(3, 2) when the source strength type is the instantaneous release. When the convective shutdown at system bottom occurred in 14,000 years in C(3, 6), the plume only spreads in the 62% of the domain in the C(3, 2). Therefore, the effects of source strength on vertical flow increase with decrease in shale layer permeability as seen in Fig. 8a, and time to convective shutdown in the model domain shortens with the continuous source release.

The source strength also affects the storage potential of the shale layers with 3×10^{-16} m^2 permeability. The increasing source strength contributes to the amount of stored

CO_2 mass in the shale layers (Fig. 8c). As opposed to the instantaneous release (C(3, 2)), 4.5 times more CO_2 was stored in the shale layers in the case C(3, 6) with continuous source supply by the end of 20,000 years as seen in Fig. 8c.

The fourth important factor that influences flow patterns and storage scheme of dissolved CO_2 is the source zone geometry. The higher interaction of brine and dissolved CO_2 at the edges of the half-length source zone in C(1, 5), C(3, 5), C(1, 7), and C(3, 7) triggers early onset of convection compared to the full-length one in C(1, 2), C(3, 2), C(1, 6), and C(3, 6), respectively. This speeds up vertical spreading for the cases with 3×10^{-14} m^2 shale layer permeability (C(1, 5) and C(1, 7)) as shown in Fig. 10. For instantaneous sources, the total CO_2mass released from the half-length source zone (C(1, 5)) is only a half of that for the full-length one (C(1, 2)). This reduces driving forces of convection due to dilution. However, we observed similar flow patterns: the plume in C(1, 5) reaches to the formation bottom at 200 years, earlier than 300 years in C(1, 2), due to faster onset of convection. For continuous source release, convective shutdown at the formation bottom occurs at 100 years in C(1, 7) with half-length source zone, while it occurs at 200 years for C(1, 6) with full-length source zone.

The faster onset of convection in the half-length source zone cases with 3×10^{-16} m^2 shale layer permeability follows the same stepwise vertical spreading with full-length source zone, as shown in Fig. 10. The homogenization of the dissolved CO_2 concentrations in the uppermost sandstone layer due to convective shutdown for the cases with continuous source release (C(3, 6) and C(3, 7)) increases CO_2 concentrations up to the solubility limit in this sandstone layer. This minimizes the effects of early convection on flow in the case C(3, 7), and the same vertical spreading pattern is observed for the half- and full-length source zone geometries with continuous source supplies as shown in Fig. 10b. The plume reaches to the formation bottom in 14,000 years for both cases. However, for instantaneous source release, the vertical flow is different for different source zone geometries, as shown in Fig. 10a. The homogenized CO_2 concentrations in the uppermost sandstone layer after convective shutdown in C(3, 5) is 50% of that in C(3, 2). Although we observe earlier onset of convection in C(3, 5), dilution and decreased concentration gradient cause decline in the driving forces of the vertical flow. The onset of convection in the second sandstone layer has not occurred in C(3, 5) at 20,000 years when the plume in C(3, 2) spreads through the fourth sandstone layer. In other words, in C(3, 5), 50% is trapped within 27% of the domain, while 100% mass is stored within 62% of the domain in C(3, 2) with full-length source zone. Therefore, the source strength and geometry of the source zone are the important factors for the flow and storage of dissolved CO_2, as well as the

permeability and thickness of the shale layers. As shown in the results in Fig. 10, the cases ran under the same initial and boundary conditions might result in different spreading patterns due to variable shale layer permeability.

Finally, the effect of continuous thin shale layers within a thick storage reservoir system can be further understood by comparing the above simulation results with those using vertical effective permeability of both sandstone and shale layers. The onset time for convection in the homogeneous domain with vertical effective permeability is delayed because the effective permeability is smaller than the sandstone permeability in the source zone of the multilayered case. For example, it takes 5 years in C(1, 3) compared to 1 year in C(1, 2), C(2, 2) and C(3, 2) with the multilayered systems (see Fig. 11). This delayed onset of convection is followed by a faster vertical flow and hence earlier convective shutdown at the formation bottom. In C(2, 3) and C(2, 2), the plume reaches the formation bottom at similar times in spite of the delayed onset of convection in C(2, 3) at 60 years. The simulation for C(3, 3) does not show an apparent convective fingering as a result of its lower effective permeability. The plume in C(3, 3) reaches the bottom of shale layers at the same time as in C(3, 2), indicating that the entire downward migration of dissolved CO_2 is control by low permeability shale layers as long as the shale permeability is low.

6. Conclusions

In this study, we investigated the effects of shale layer and source zone properties on flow and storage of dissolved CO_2 in a multilayered storage system. The key findings from this study are summarized below:

1. The presence of any relatively low permeability shale layer interbedded between relatively higher permeability sandstone layers in a storage formation slows down the vertical flow, and alters the storage scheme of dissolved CO_2. The cases with the same initial and boundary conditions might result in different spreading patterns due to variations in the shale layer permeability and thickness.
2. The decrease in permeability and increase in thickness of the shale layers result in stable and long-term trapping in smaller storage volumes in the upper sandstone and shale layers, when compared to the whole domain for homogeneous cases.
3.

The higher the shale permeability is and the thinner the shale layer is, the more dominant the convective mixing is. The trapping strategy should be to increase the contact area between dissolved CO_2 and the host rock, and the residence time to enhance potential for mineralization.

4.

The occurrence of convective shutdown and the onset of convection in the deeper sandstone layers in a multilayered system depend on the permeability and thickness of the shale layers, as well as the source strength and geometry of the source zone.

5.

The onset of convection is delayed by continuous source release compared to instantaneous release. The time to convective shutdown in the model domain shortens with the continuous source release. The effects of source strength on vertical flow increase with decreasing shale layer permeability.

6.

The onset of convection is earlier with half-length source zone due to increasing brine and dissolved CO_2 interactions compared to full-length source zone. The vertical flow pattern and timing of the transport for these source zone geometries with instantaneous and continuous source releases strongly depend on the permeability of the shale layers.

7.

The comparison with those cases having effective vertical permeability for both sandstone and shale layers indicates that it is important to capture the discrete continuous thin shale layers in a storage system and include these layers in the modeling of convective mixing for dissolution trapping and mineralization trapping.

Based on these findings, the presence of shale layers in a storage formation may be beneficial to the stable trapping of dissolved CO_2 as these shale layers enhance lateral spreading and concentration homogenization in sandstone layers. In addition, the dissolved CO_2 can be stably trapped in the shale layers for a long time. On the other hand, convective mixing leads plume to spread vertically through the deeper parts of the homogeneous formation. Having higher vertical permeability should be advantageous to allow faster dissolution and onset of convection. This will contribute to the storage of dissolved CO_2 in the deeper parts of the formation. As a conclusion, the storage strategy

should be site specific, which should be developed by considering geological properties of the formation.

Acknowledgments

This research is funded by National Science Foundation grant number EAR-1045282 and Department of Energy grant number DE-FE0004630 through National Energy Technology Laboratory. For access to the data included in this paper for research purposes, please contact the corresponding author.

Appendix A. Model verification with the Elder problem

The numerical model was verified with the Elder benchmark problem. Elder (1967) experimentally studied thermally driven convection in a closed rectangular box shaped vertical model. The flow in the box was initiated by a vertical temperature gradient. In the numerical modeling study, Elder (1967)employed a finite difference representation of the governing equations for vorticity, stream function, and thermal energy balance. Eighty lateral and forty vertical nodes were used, and time discretization was set to reach the first point of the comparison (1 year) in 20 time steps (Hassanzadeh et al., 2005, Simpson and Clement, 2003). Voss and Souza (1987) modified the Elder problem into a variable density groundwater flow, where the fluid density was as a function of salt concentration. We used similar approach with Voss and Souza (1987) to verify our model.

We assumed that solute and heat transport in porous media are governed by similar balance equations using an analogy between Fourier's law for conduction and Fick's law for diffusion. We solved the Elder problem in terms of salt mass concentration for a saltwater intrusion problem in a homogeneous porous medium initially saturated with fresh water. 2-D study domain was 600 m in length and 300 m in height. A 300 m long source with “1” relative salt mass fraction (w_1) was placed to the middle of the top boundary as a fixed concentration boundary condition (Fig. 12a). Zero salt mass fraction (w_2) was applied to the entire bottom boundary. The other sides of the domain were set as no flow and no mass flux boundary conditions (Simpson and Clement, 2003). At each upper corner, 1 atm pressure was specified, and an initial pressure was hydrostatic. Simulation parameters for the Elder problem are given in Table 3. In the simulations, 160 lateral and 80 vertical grid cells were used, and time step was adaptively changed with a maximum set to 1 month.

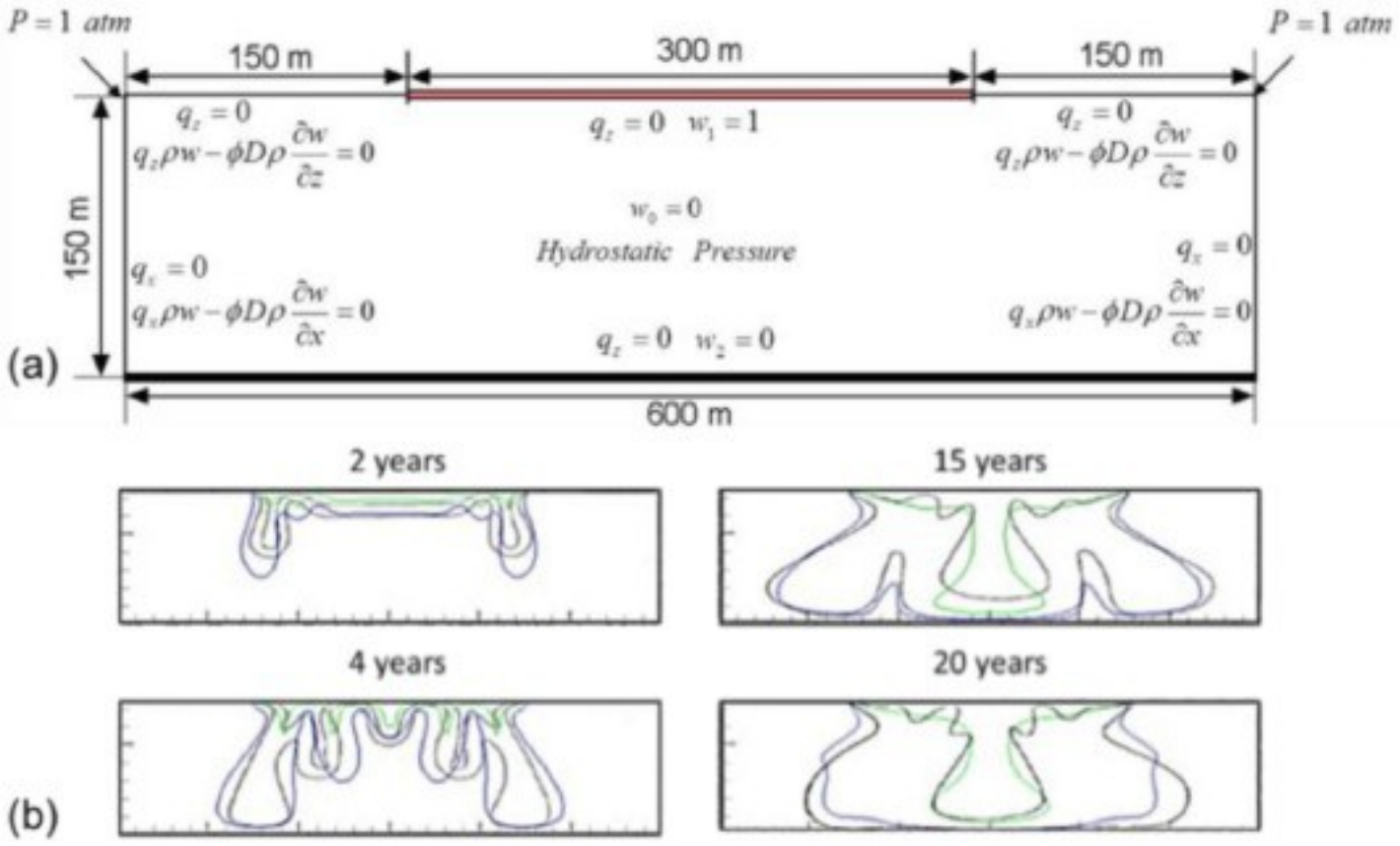

1. Download high-res image (247KB)
2. Download full-size image

Fig. 12. (a) Initial and boundary conditions for the Elder problem; (b) comparison of our results (blue lines for 0.2 w/w_1 and green lines for 0.6 w/w_1) with the Elder's results (1967) (black lines for 0.2 and 0.6 w/w_1).

Table 3. Simulation parameters for the Elder problem (Voss and Souza, 1987).

Parameter	Value
Permeability, k (m^2)	4.845×10^{-13}
Porosity, ϕ (−)	0.10
Diffusion coefficient, D (m^2/s)	3.565×10^{-6}

As the salt (w_1) diffuses into fresh water from the source zone, the density of the fluid mixture increases and as shown in Fig. 12b, the denser salty water tend to sink forming density-driven convective fingers. Fig. 12b shows that our numerical model predictions are generally in agreement with the results based on the numerical solution of Elder (1967), although there are slight differences, which could be due to different solution method, time steps and numerical converge criteria used in the two different models.

Appendix B. Sensitivity analysis of model parameters

Before the application of the model to a field-scale study, sensitivity of the grid resolution and fluctuation strength of porosity and permeability on the solution were investigated for the same small tank test setting (Figs. 1 and 13) and surrogate fluid combination with Agartan et al. (2015). The experiments were conducted under ambient pressure and temperature conditions using food dyed water and propylene glycol having similar density characteristics as $CO_2$and brine, respectively (see the graph in Fig. 1 in Agartan et al. (2015)).

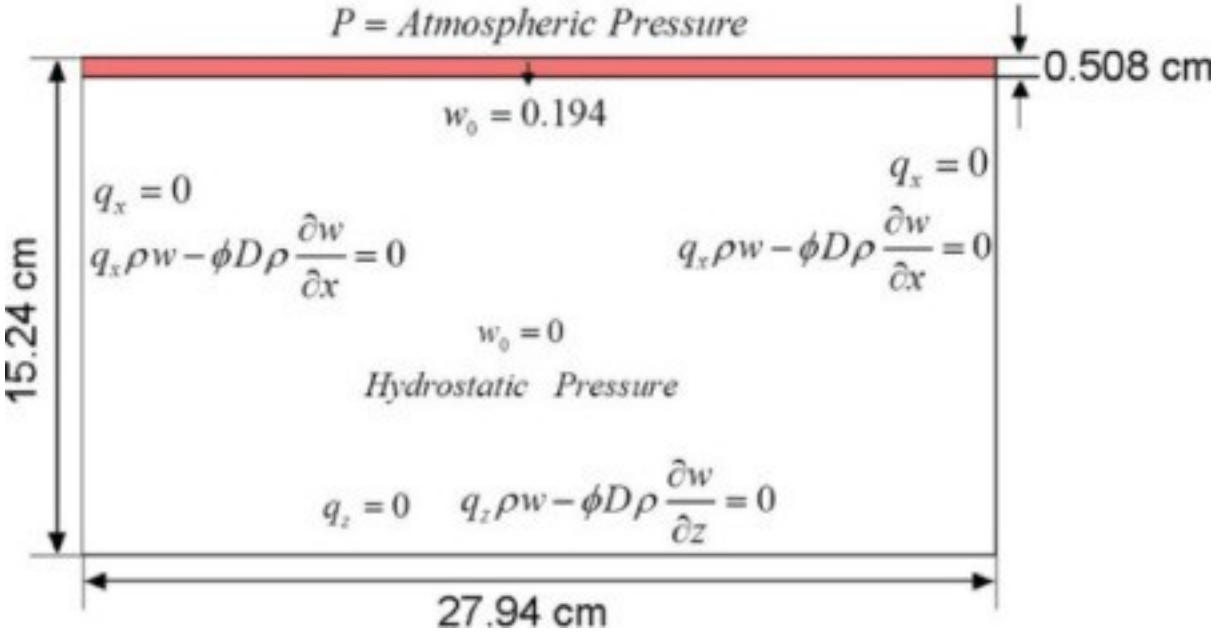

1. Download high-res image (153KB)
2. Download full-size image

Fig. 13. Initial and boundary conditions of the numerical model (not to scale).

Pau et al., 2009, September, Pau et al., 2010 investigated the influences of simulation parameters, such as grid resolution, porosity and permeability fluctuations, solver tolerances, and domain size, on the solution using a block-structured adaptive mesh refinement method. They assumed a 2-D isothermal and homogeneous domain with a layer of CO_2-saturated brine at the top of the domain. The focus of their study is on understanding the dependence of stabilized mass flux from the source zone and onset time of convection on the simulation parameters mentioned above. The porosity or permeability fluctuations were added to the model to overcome the numerical errors associated with the solution space. They found that the onset time decreases with increasing magnitudes of the porosity and permeability fluctuations, however the onset of fingering is more sensitive to porosity fluctuations. We followed a similar approach

here as discussed below to examine the sensitivity of the simulation parameters and then to decide on appropriate range of parameters for our analyses.

The domain with 27.94 cm × 15.24 cm × 2.54 cm (length × height × width) was fully saturated with propylene glycol as an analog of brine. An initial mass fraction of water as an analog of CO_2-charged brine in the 0.508 cm thick source zone was assumed to be 0.194. The density and viscosity of propylene glycol solutions are functions of water mass fraction as given in Eqs. (7) and (8), respectively (Agartan et al., 2015). The boundary condition at the top was specified as constant pressure equal to the atmospheric pressure, and no flux boundary condition was assumed for water. As the tank was a closed system, no flow boundary conditions for pressure and water concentration were assigned to the other boundaries.

The effects of 1, 2, 5, 10, and 25% porosity and permeability fluctuations on the onset time for convection were examined. The results in Fig. 14a indicate the influences of heterogeneity in porosity and permeability on convection. The onset time for convective fingering decreases significantly with increasing fluctuation in porosity and permeability because the spatial distribution of these properties in the formation triggers finger generation. The effects of fluctuations on the fingering decreases with increasing fluctuations. However, the onset time is more sensitive to the porosity fluctuation than the permeability fluctuation.

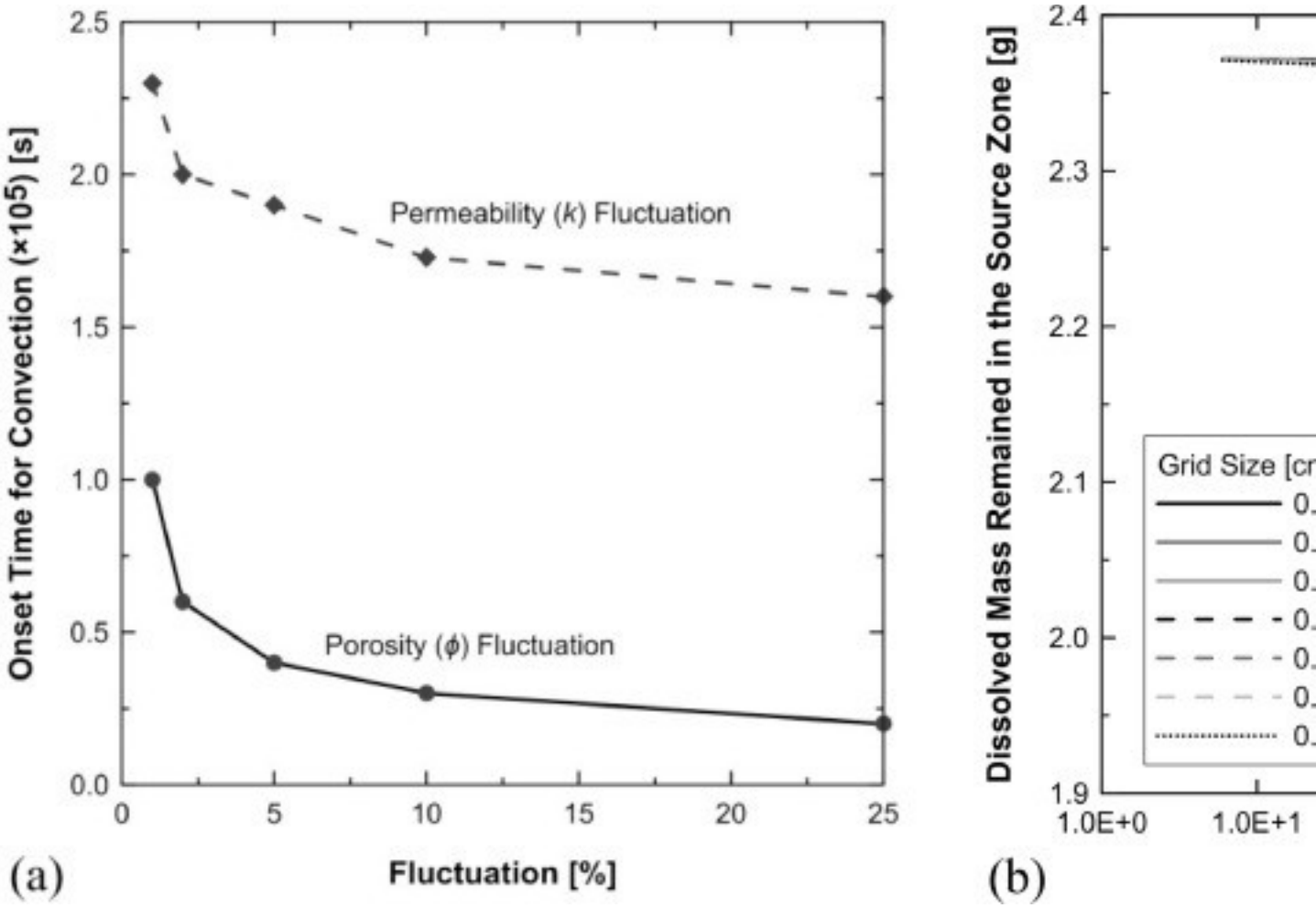

1. Download high-res image (359KB)
2. Download full-size image

Fig. 14. Effects of (a) porosity (ϕ) and permeability (k) fluctuations and (b) grid resolution on the onset time for convection.

The grid resolution study was carried out to determine the critical grid size to capture the experimental observations accurately while minimizing the numerical errors. The grid size should be smaller than the critical wavelength (λ_c) of the convective finger to capture the initiation of convection accurately (Riaz et al., 2006). λ_c derived from the linear stability analysis by Riaz et al. (2006) was used to examine the onset of convection. λ_c was calculated to be 1.770 cm for the simulation parameters in Table 4. We selected grid sizes smaller than the λ_c, and assigned a porosity fluctuation to each grid size. We followed similar approach with Pau et al. (2009) where when the grid size was reduced by half, its corresponding porosity fluctuation was doubled to get a better convergence (0.5080 cm – 0.25%, 0.2540 cm – 0.50%, 0.1270 cm – 1.00%, 0.0847 cm – 1.50%, 0.0635 cm – 2.00%, 0.0508 cm – 2.50%, and 0.0423 cm – 3.00%. The

variation in the dissolved mass remained in the source zone with time was examined for each grid resolution and the associated porosity fluctuations (Fig. 14b). The results show that the amount of the dissolved mass remained in the source zone converges to a single value for the grid resolutions equal or smaller than 0.0635 cm and porosity fluctuations equal or greater than 2%. On the other hand, significant variations in the mass in the source zone were observed for the larger grid resolutions because the corresponding porosity fluctuations were not adequate to overcome numerical errors that can result in false generation of fingering. The numerical model is not sensitive to the solver tolerances.

Table 4. Fluid and formation properties.

Parameter	Value
Density of PG, ρ_{PG} (kg/m^3)	1034.1
Viscosity of PG, μ_{PG} (Pa.s)	0.055
Density of water, ρ_w (kg/m^3)	1000
Viscosity of water, μ_w (Pa.s)	0.001
Permeability, k (m^2)	1.079×10^{-10}
Effective diffusion coefficient, D_{eff} (m^2/s)	8.0×10^{-11}
Porosity, ϕ (−)	0.325
Mass fraction of water, w (−)	0.194
Density increase due to water dissolution, $\Delta\rho$ (kg/m^3)	9.1
Gravitational acceleration, g (m/s^2)	9.81

References

Agartan Karacaer, 2015

E. Agartan Karacaer**A Fundamental Study on the Effects of Heterogeneity on Trapping of Dissolved CO_2 in Deep Geological Formations through Intermediate-scale Testing and Numerical Modeling**

Colorado School of Mines (2015), p. 204

View Record in Scopus

Agartan et al., 2015

E. Agartan, L. Trevisan, A. Cihan, B. Birkholzer, Q. Zhou, T.H. Illangasekare**Experimental study on effects of geologic heterogeneity in enhancing dissolution trapping of supercritical CO_2**

Water Resour. Res., 51 (3) (2015), pp. 1635-1648, 10.1002/2014WR015778

CrossRefView Record in Scopus

Arts et al., 2008

R.J. Arts, A. Chadwick, O. Eiken, S. Thibeau, S. Nooner**Ten years' experience of monitoring CO_2 injection in the Utsira Sand at Sleipner, offshore Norway**
First break, 26 (1) (2008)

Bachu, 2008

S. Bachu**CO_2 storage in geological media: role, means, status and barriers to deployment**
Prog. Energy Combust. Sci., 34 (2) (2008), pp. 254-273, 10.1016/j.pecs.2007.10.001
ArticleDownload PDFView Record in Scopus

Backhaus, 2011

S. Backhaus, K. Turitsyn, R.E. Ecke**Convective instability and mass transport of diffusion layers in Hele-Shaw geometry**
Phys. Rev. Lett., 106 (2011), p. 104501, 10.1103/PhysRevLett.106.104501
CrossRef

Bear, 1972

J. Bear**Dynamics of Fluids in Porous Media**
London and Amsterdam: American Elsevier, New York (1972)

Benson and Cook, 2005

S.M. Benson, P. Cook**Underground Geological Storage, in Intergovernmental Panel on Climate Change Special Report on Carbon Dioxide Capture and Storage. Coordinating author P. Freund**
Cambridge Univ. Press, Cambridge, U. K (2005), pp. 195-276
View Record in Scopus

Bradshaw et al., 2007

J. Bradshaw, S. Bachu, D. Bonijoly, R. Burruss, S. Holloway, N.P.Christensen, O.M. Mathiassen**C O_2 storage capacity estimation: issues and development of standards**
Int. J. Greenhouse Gas Control, 1 (1) (2007), pp. 62-68, 10.1016/S1750-5836(07)00027-8
ArticleDownload PDFView Record in Scopus

Chadwick et al., 2004

R.A. Chadwick, R. Arts, O. Eiken, G.A. Kirby, E. Lindeberg, P. Zweigel**4D seismic imaging of an injected CO_2 plume at the sleipner field, central North Sea, Geological Society of London**
Richard J. Davies (Ed.), 3D Seismic Technology: Application to the Exploration of Sedimentary Basins, Geological Society of London, London, UK (2004), pp. 311-320
Geological Society of London Memoir, 29, http://dx.doi.org/10.1144/GSL.MEM.2004.029.01.29
CrossRefView Record in Scopus

Chapman and Parker, 2005

S.W. Chapman, B.L. Parker**Plume persistence due to aquitard back diffusion following dense nonaqueous phase liquid source removal or isolation**
Water Resour. Res., 41 (12) (2005), p. W12411, 10.1029/2005WR004224

Chapman et al., 2012

S.W. Chapman, B.L. Parker, T.C. Sale, L.A. Doner**Testing high resolution numerical models for analysis of contaminant storage and release from low permeability zones**
J. Contam. Hydrol., 136 (2012), pp. 106-116, 10.1016/j.jconhyd.2012.04.006
ArticleDownload PDFView Record in Scopus

Cihan et al., 2011

A. Cihan, Q. Zhou, J.T. Birkholzer**Analytical solutions for pressure perturbation and fluid leakage through aquitards and wells in multilayered-aquifer systems**
Water Resour. Res., 47 (10) (2011), 10.1029/2011WR010721

De Silva et al., 2012

P.N.K. De Silva, P.G. Ranjith, S.K. Choi**A study of methodologies for CO_2 storage capacity estimation of coal**
Fuel, 91 (1) (2012), pp. 1-15, 10.1016/j.fuel.2011.07.010
ArticleDownload PDFView Record in Scopus

Duan - and - Sun, - 2003

Z. Duan, R. Sun**An improved model calculating CO_2 solubility in pure water and aqueous NaCl solutions from 273 to 533 K and from 0 to 2000 bar**
Chem. Geol., 193 (3) (2003), pp. 257-271, 10.1016/S0009-2541(02)00263-2
ArticleDownload PDFView Record in Scopus

Duan et al., 2006

Z. Duan, R. Sun, C. Zhu, I. Chou**An improved model for the calculation of CO_2 solubility in aqueous solutions containing Na+, K+, Ca2+, Mg2+, Cl−, and SO42-**
Mar. Chem., 98 (2) (2006), pp. 131-139, 10.1016/j.marchem.2005.09.001
ArticleDownload PDFView Record in Scopus

Elder, 1967

J.W. Elder**Steady free convection in a porous medium heated from below**
J. Fluid Mech., 27 (1) (1967), pp. 29-48
CrossRefView Record in Scopus

Elenius and Gas 2013

M.T. Elenius, S.E. Gasda**Convective mixing in formations with horizontal barriers**
Adv. Water Res., 62 (2013), pp. 499-510, 10.1016/j.advwatres.2013.10.010
ArticleDownload PDFView Record in Scopus

Emami-Meybodi

H. Emami-Meybodi, H. Hassanzadeh, C.P. Green, J. Ennis-King**Convective dissolution of CO_2 in saline aquifers: progress in modeling and experiments**
Int. J. Greenhouse Gas Control, 40 (2015), pp. 238-266
ArticleDownload PDFView Record in Scopus

Farajzadeh et al.

R. Farajzadeh, F.F. Zinati, P.L.J. Zitha, J. Bruining**Density-driven natural convection in dual layered and anisotropic porous media with application for CO_2 injection projects**
Paper Presented at 11th European Conference on the Mathematics of Oil Recovery, Bergen, Norway (2008)

Farajzadeh et al.

R. Farajzadeh, P. Ranganathan, P.L.J. Zitha, J. Bruining**The effect of heterogeneity on the character of density-driven natural convection of CO_2 overlying a brine layer**
Adv. Water Res., 34 (3) (2011), pp. 327-339
ArticleDownload PDFView Record in Scopus

Green and Ennis

C.P. Green, J. Ennis-King**Effect of vertical heterogeneity on long-term migration of CO_2 in saline formations**
Transp. Porous Media, 82 (1) (2010), pp. 31-47, 10.1007/s11242-009-9498-7
CrossRefView Record in Scopus

Green et al., 200

C.P. Green, J. Ennis-King, K. Pruess**Effect of vertical heterogeneity on long-term migration of CO_2 in saline formation**

Energy Procedia, 1 (1) (2009), pp. 1823-1830
ArticleDownload PDFView Record in Scopus

Grimstad et al., 2

A.A. Grimstad, S. Georgescu, E. Lindeberg, J.F. Vuillaume**Modelling and simulation of mechanisms for leakage of CO_2 from geological storage**
Energy Procedia, 1 (1) (2009), pp. 2511-2518, 10.1016/j.egypro.2009.02.014
ArticleDownload PDFView Record in Scopus

Hassanzadeh et

H. Hassanzadeh, M. Pooladi-Darvish, D. Keith**Modeling of convective mixing in CO_2 storage**
J. Can. Pet. Technol., 44 (10) (2005)

Hassanzadeh et

H. Hassanzadeh, M. Pooladi-Darvish, D.W. Keith**Scaling behavior of convective mixing, with application to geological storage of CO_2**
AIChE J., 53 (5) (2007), pp. 1121-1131, 10.1002/aic.11157
CrossRefView Record in Scopus

Herrera et al., 20

Herrera, P.A., Nordbotten, J.M., El-Faour, B.F., Keilegavlen, E., Dahle, H.K., 2010. The impact of natural heterogeneity on CO_2 migration deep saline aquifers.

Hewitt et al., 201

D.R. Hewitt, J.A. Neufeld, J.R. Lister**Convective shutdown in a porous medium at high Rayleigh number**
J. Fluid Mech., 719 (2013), pp. 551-586, 10.1017/jfm.2013.23
CrossRefView Record in Scopus

Hewitt et al., 201

D.R. Hewitt, J.A. Neufeld, J.R. Lister**High Rayleigh number convection in a three-dimensional porous medium**
J. Fluid Mech., 748 (2014), pp. 879-895, 10.1017/jfm.2014.216
CrossRefView Record in Scopus

Illangasekare et

T. Illangasekare, S.W. Tyler, T.P. Clement, K.G. Villholth, A.P.G.R.L.Perera, J. Obeysekera, A. Gunatilaka, C.R. Panabokke, D.W. Hyndman, K.J.Cunningham, J.J. Kaluarachchi, W.W.-G. Yeh, M.T. van Genuchten, K. Jensen**Impacts of the 2004 tsunami on groundwater resources in Sri Lanka**
Water Resour. Res., 42 (5) (2006), 10.1029/2006WR004876

Johnson et al., 2

J.W. Johnson, J.J. Nitao, K.G. Knauss**Reactive transport modeling of CO_2 storage in saline aquifers to elucidate fundamental processes, trapping mechanisms and sequestration partitioning**
Geol. Storage Carbon Dioxide, 233 (2004), pp. 107-128

CrossRefView Record in Scopus

Konikow and Ne

L.F. Konikow, C.E. Neuzil**A method to estimate groundwater depletion from confining layers**
Water Resour. Res., 43 (2007), p. W07417, 10.1029/2006WR005597

Li et al., 2016

C. Li, K. Zhang, Y. Wang, C. Guo, F. Maggi**Experimental and numerical analysis of reservoir performance for geological CO_2storage in the Ordos Basin in China**
Int. J. Greenhouse Gas Control, 45 (2016), pp. 216-232
ArticleDownload PDFView Record in Scopus

Lindeberg et al.,

E. Lindeberg, E. Causse, A. Ghaderi**SINTEF Petroleum Research Report 54.5148. 00/01/99**
(1999), p. 13
Restricted
View Record in Scopus

Lindeberg and B

E. Lindeberg, P. Bergmo**The long-term fate of CO_2 injected into an aquifer**
Greenhouse Gas Control Technol., 1 (2003), pp. 489-494
ArticleDownload PDFView Record in Scopus

McKibbin and O'

R. McKibbin, M.J. O'Sullivan**Onset of convection in a layered porous medium heated from below**
J. Fluid Mech., 96 (Part 2) (1980), pp. 375-393
CrossRefView Record in Scopus

McKibbin and Ty

R. McKibbin, P.A. Tyvand**Anisotropic modelling of thermal convection in multilayered porous media**
J. Fluid Mech., 118 (1) (1982), pp. 315-339
CrossRefView Record in Scopus

McKibbin, 1986

R. McKibbin**Heat transfer in a vertically-layered porous medium heated from below**
Transp. Porous Media, 1 (4) (1986), pp. 361-370
View Record in Scopus

Nicot, 2008

J.P. Nicot**Evaluation of large-scale carbon storage on fresh-water section of aquifers: a Texas study**
Int. J. Greenhouse Gas Control, 2 (4) (2008), pp. 582-593, 10.1016/j.ijggc.2008.03.004
ArticleDownload PDFView Record in Scopus

Nield and Simm

D.A. Nield, C.T. Simmons**A discussion on the effect of heterogeneity on the onset of convection in a porous medium**
Transp. Porous Media, 68 (3) (2007), pp. 413-421
CrossRefView Record in Scopus

Nooner et al., 20

S.L. Nooner, O. Eiken, C. Hermanrud, G.S. Sasagawa, T. Stenvold, M.A.Zumberge**Constraints on the in situ density of CO_2 within the Utsira formation from time-lapse seafloor gravity measurements**
Int. J. Greenhouse Gas Control, 1 (2) (2007), pp. 198-214, 10.1016/S1750-5836(07)00018-7
ArticleDownload PDFView Record in Scopus

Parker et al., 200

B.L. Parker, J.A. Cherry, S.W. Chapman**Field study of TCE diffusion profiles below DNAPL to assess aquitard integrity**
J. Contam. Hydrol., 74 (1) (2004), pp. 197-230, 10.1016/j.jconhyd.2004.02.011
ArticleDownload PDFView Record in Scopus

Parker et al., 200

B.L. Parker, S.W. Chapman, M.A. Guilbeault**Plume persistence caused by back diffusion from thin clay layers in a sand aquifer following TCE source-zone hydraulic isolation**
J. Contam. Hydrol., 102 (1) (2008), pp. 86-104, 10.1016/j.jconhyd.2008.07.003
ArticleDownload PDFView Record in Scopus

Pau et al., 2009,

G.S. Pau, J.B. Bell, K. Pruess, A.S. Almgren, M.J. Lijewski, K.Zhang**Numerical studies of density-driven flow in CO_2 storage in saline aquifers**
Procedings Tough Workshop, Lawrence Berkeley National Laboratory, September, Berkeley, California (2009)

Pau et al., 2010

G.S. Pau, J.B. Bell, K. Pruess, A.S. Almgren, M.J. Lijewski, K. Zhang**High-resolution simulation and characterization of density-driven flow in CO_2storage in saline aquifers**
Adv. Water Res., 33 (4) (2010), pp. 443-455, 10.1016/j.advwatres.2010.01.009
ArticleDownload PDFView Record in Scopus

Phillips et al., 19

S.L. Phillips, A. Igbene, J.A. Fair, H. Ozbek, M. Tavana**Lawrence Berkeley National Laboratory Report LBL-12810, Berkeley, CA**
(1981)

Raad and Hassa

S.M.J. Raad, H. Hassanzadeh**Onset of dissolution-driven instabilities in fluids with nonmonotonic density profile**
Phys. Rev. E, 92 (5) (2015), Article 053023

Raad et al., 2016

S.M. Raad, H. Emami-Meybodi, H. Hassanzadeh**On the choice of analogue fluids in CO_2 convective dissolution experiments**
Water Resour. Res., 52 (2016), pp. 4458-4468, 10.1002/2015WR018040

Ranganathan et al., 2012
P. Ranganathan, R. Farajzadeh, H. Bruining, P.L. Zitha**Numerical simulation of natural convection in heterogeneous porous media for CO_2 geological storage**
Transp. Porous Media, 95 (1) (2012), pp. 25-54
CrossRefView Record in Scopus

Riaz et al., 2006
A. Riaz, M. Hesse, H.A. Tchelepi, F.M. Orr**Onset of convection in a gravitationally unstable diffusive boundary layer in porous media**
J. Fluid Mech., 548 (1) (2006), pp. 87-111, 10.1017/S0022112005007494
CrossRefView Record in Scopus

Sakaki and Illangasekare, 2007
T. Sakaki, T.H. Illangasekare**Comparison of height-averaged and point-measured capillary pressure-saturation relations for sands using a modified Tempe cell**
Water Resour. Res., 43 (2007), p. 6, 10.1029/2006WR005814

Schincariol and Schwartz, 1990
R.A. Schincariol, F.W. Schwartz**An experimental investigation of variable density flow and mixing in homogeneous and heterogeneous media**
Water Resour. Res., 26 (10) (1990), pp. 2317-2329, 10.1029/WR026i010p02317
CrossRefView Record in Scopus

Schincariol et al., 1994
R.A. Schincariol, F.W. Schwartz, C.A. Mendoza**On the generation of instabilities in variable density flow**
Water Resour. Res., 30 (4) (1994), pp. 913-927
CrossRefView Record in Scopus

Schroth et al., 1996
M.H. Schroth, J.D. Istok, S.J. Ahearn, J.S. Selker**Characterization of Miller-similar silica sands for laboratory hydrologic studies**
Soil Sci. Soc. Am. J., 60 (5) (1996), pp. 1331-1339
CrossRefView Record in Scopus

Simpson and Clement, 2003
M.J. Simpson, T.P. Clement**Theoretical analysis of the worthiness of Henry and Elder problems as benchmarks of density-dependent groundwater flow models**
Adv. Water Res., 26 (1) (2003), pp. 17-31, 10.1016/S0309-1708(02)00085-4
ArticleDownload PDFView Record in Scopus

Smits et al., 2010

K.M. Smits, T. Sakaki, A. Limsuwat, T.H. Illangasekare**Thermal conductivity of sands under varying moisture and porosity in drainage–wetting cycles**
Vadose Zone J., 9 (1) (2010), pp. 172-180, 10.2136/vzj2009.0095
CrossRefView Record in Scopus

Torp and Gale, 2004
T.A. Torp, J. Gale**Demonstrating storage of CO_2 in geological reservoirs: the Sleipner and SACS projects**
Energy, 29 (9) (2004), pp. 1361-1369
ArticleDownload PDFView Record in Scopus

van der Meer, 1993
L.G.H. van der Meer**The conditions limiting CO_2 storage in aquifers**
Energy Convers. Manage., 34 (9) (1993), pp. 959-966, 10.1016/0196-8904(93)90042-9
ArticleDownload PDFView Record in Scopus

Vithanage et al., 2012
M. Vithanage, P. Engesgaard, K.H. Jensen, T.H. Illangasekare, J.Obeysekera**Laboratory investigations of the effects of geologic heterogeneity on groundwater salinization and flush-out times from a tsunami-like event**
J. Contam. Hydrol., 136 (2012), pp. 10-24, 10.1029/WR023i010p01851
ArticleDownload PDFView Record in Scopus

Voss and Souza, 1987
C.I. Voss, W.R. Souza**Variable density flow and solute transport simulation of regional aquifers containing a narrow freshwater-saltwater transition zone**
Water Resour. Res., 23 (10) (1987), pp. 1851-1866
CrossRefView Record in Scopus

Wietsma et al., 2009
T.W. Wietsma, M. Oostrom, M.A. Covert, T.E. Queen, M.J. Fayer**An automated tool for three types of saturated hydraulic conductivity laboratory measurements**
Soil Sci. Soc. Am. J., 73 (2) (2009), pp. 466-470
CrossRefView Record in Scopus

Wilking et al., 2012
B.T. Wilking, D.R. Rodriguez, T.H. Illangasekare**Experimental study of the effects of DNAPL distribution on mass rebound**
Ground Water, 51 (2) (2012), pp. 229-236, 10.1111/j.1745-6584.2012.00962.x

Zhang et al., 2008
C. Zhang, C.J. Werth, A.G. Webb**Investigation of surfactant-enhanced mass removal and flux reduction in 3D correlated permeability fields using magnetic resonance imaging**
J. Contam. Hydrol., 100 (3) (2008), pp. 116-126
ArticleDownload PDFView Record in Scopus

Zhang et al., 2016

K. Zhang, J. Xie, C. Li, L. Hu, X. Wu, Y. Wang**A full chain CCS demonstration project in northeast Ordos Basin, China: operational experience and challenges**
Int. J. Greenhouse Gas Control, 50 (2016), pp. 218-230
ArticleDownload PDFView Record in Scopus

Zweigel et al., 2004
P. Zweigel, R. Arts, A.E. Lothe, E.B. Lindeberg

Reservoir Geology of the Utsira Formation at the First Industrial-Scale Underground CO_2Storage Site (Sleipner Area, North Sea), 233, Geological Society, London, Special Publications (2004), pp. 165-180
CrossRefView Record in Scopus